



# Modeling of fracture in small punch tests for small- and large-scale yielding conditions at various temperatures



C. Soyarslan <sup>a,\*</sup>, B. Gülçimen <sup>b</sup>, S. Bargmann <sup>a,c</sup>, P. Hähner <sup>d</sup>

<sup>a</sup> Institute of Continuum and Material Mechanics, Hamburg University of Technology, 21073 Hamburg, Germany

<sup>b</sup> Department of Mechanical Engineering, Uludağ University, Görükle, 16059 Bursa, Turkey

<sup>c</sup> Institute of Materials Research, Helmholtz-Zentrum Geesthacht, 21502 Geesthacht, Germany

<sup>d</sup> Institute for Energy and Transport, Joint Research Centre, European Commission, P.O. Box 2, 1755 ZG Petten, The Netherlands

## ARTICLE INFO

### Article history:

Received 21 September 2015

Received in revised form

5 November 2015

Accepted 10 December 2015

Available online 18 December 2015

### Keywords:

Ductile–brittle transition

Small punch test

Gurson–Tvergaard–Needleman plasticity

Ritchie–Knott–Rice model

## ABSTRACT

We present a systematic numerical study on temperature dependent fracture mode change in small punch tests. Following Needleman and Tvergaard (2000), we model the material as thermo-inelastic, where the ductile fracture mode, by void nucleation, growth and coalescence is accounted for by Gurson's porous metal plasticity (Gurson, 1977). The brittle fracture mode by cleavage is accounted for by Ritchie–Knott–Rice's deterministic maximum principal stress criterion (Ritchie et al., 1973). The well-known problem of mesh dependence associated with softening material behavior is remedied by using an integral type nonlocal formulation similar to that presented in Tvergaard and Needleman (1995). Two length scales are incorporated into the constitutive relations: the ductile fracture length scale is based on the average inclusion distance and associated with the nonlocal evolution equation for the porosity. The brittle fracture length scale is based on the average grain size and associated with the material region at which the maximum principal stress is averaged out. The material model is used to simulate small punch tests at  $-196\text{ }^{\circ}\text{C}$ ,  $-158\text{ }^{\circ}\text{C}$  and  $25\text{ }^{\circ}\text{C}$  of notched and unnotched specimens of P91 steel representative for small- and large-scale yielding conditions, respectively. The simulated fracture modes and patterns show a very good agreement with experiments: for  $-196\text{ }^{\circ}\text{C}$  brittle fracture propagating normal to the maximum (tensile) principal stress prevails. For  $25\text{ }^{\circ}\text{C}$  ductile fracture is governed by shear localization with voidage. The simulations also show that the deformation energy is considerably higher for the upper shelf tests compared to the lower shelf tests.

© 2015 The Authors. Published by Elsevier Ltd. This is an open access article under the CC BY-NC-ND license (<http://creativecommons.org/licenses/by-nc-nd/4.0/>).

## 1. Introduction

The ductile–brittle transition, typically seen in bcc and hcp metals, involves a change of fracture mode as a function of test temperature and/or loading rate. Brittle fracture occurs by cleavage along specific crystallographic planes at lower temperatures, associated with the lower shelf in deformation energy, whereas ductile fracture goes along with progressive cavitation until void coalescence at higher temperatures, associated with the upper shelf. The temperature at which the prevailing mode of failure changes from brittle to ductile is named ductile–brittle transition temperature.

At a finer scale this transition is explained by minute energetic requirements for the evolution of the defect structure. Once certain conditions are met, brittle propagation of a sharp crack front with free surface development and atomic bond rupture is favored over dislocation emission and/or mobility and concomitant crack tip blunting.

Brittle fracture is referred to as a low energy fracture, whereas ductile fracture is a high energy fracture since the overall process zone is larger due to crack blunting and plastic zone development. Ductile fracture by void growth occurs under relatively large strains as compared to brittle fracture in which the driving mechanism is the critical stress over the cleavage grain (see, e.g., [1]). As the flow stress is temperature and rate dependent, large stresses needed for brittle fracture are achieved only for low temperatures and/or high strain rates; otherwise ductile fracture at high strains is observed.

In the present work, we model the ductile–brittle transition at the macroscale in small punch tests at various temperatures. Small punch testing was first developed in the early 1980s for determining the post-irradiation mechanical properties including ductile–brittle transition temperature [2]. The method possesses great advantage over the conventional Charpy test due to the small amount of material needed. Small punch specimens are usually disk-shaped with thicknesses in the range of 0.25–0.5 mm and diameters of 3–10 mm. Therefore, the test is virtually non-destructive, and samples can even be extracted from big components in service. Owing to this reduced material requirement, small punch testing is also

\* Corresponding author. Tel.: +49 40878 2562, +49 42878 2562.

E-mail address: [celal.soyarslan@tuhh.de](mailto:celal.soyarslan@tuhh.de) (C. Soyarslan).

applied when sampling volume is limited, for instance, to the heat affected zone of a weldment [3]. In previous works, it was reported that the transition temperatures determined by small punch tests were considerably lower than the ones determined by Charpy tests [4–7]. A linear correlation between the small punch transition temperature and the conventional ductile–brittle transition temperature was proposed in the European Code of Practice of small punch testing [8]. Possible reasons for the discrepancy were attributed to the stress triaxiality, size and strain rate effects.

Despite the wide range of literature on the transition temperature as determined by small punch testing, there has been no attempt to assess the ductile and brittle crack patterns as well as the transition temperature in a unified numerical framework. Following the lines of Needleman and Tvergaard [1], we use temperature coupled Gurson–Tvergaard–Needleman porous metal visco-plasticity for modeling the ductile fracture involving progressive cavitation with the recent shear modification by [9]. The brittle fracture is modeled deterministically following the Ritchie–Knott–Rice (RKR) model [10]. The motivation for the selection of a porous metal plasticity model stems from the experimental evidence of cavitation on fracture surfaces. Physically, ductile and brittle fractures are nonlocal processes with interacting sources of disorder at various length scales. Thus, a nonlocal formulation is required with incorporation of length scales. Through that an accurate control of the size of the localization zone (important in consideration of the size effects) on the course of deformation is supplied. In addition, the problem of pathological mesh dependence of the numerical simulations is removed.

The model is validated by comparisons between the numerical analysis and experimental results obtained at  $-196^\circ\text{C}$ ,  $-158^\circ\text{C}$  and  $25^\circ\text{C}$ . Notched and unnotched specimen geometries are simulated corresponding to the small- and large-scale yielding conditions, respectively. The experimental evaluation of the  $J$ – $R$  ( $J$  resistance) curves for P91 shows that the transition temperature is around  $-150^\circ\text{C}$  based on experimental and numerical load–displacement curves as well as optical and SEM images revealing the crack patterns and fracture surface morphologies. It is shown that, as anticipated, for both notched and unnotched tests ductile fracture at the upper shelf follows the plastic localization bands whose sizes are of the order of magnitude of the utilized length scale. This amounts to a mixed Mode I and Mode II fracture. Brittle cracks propagate under Mode I conditions in the direction normal to the maximum principal stress, with small-scale yielding prevailing at the crack tip. This is in agreement with the experimental observation of cleavage facets orthogonal to the maximum principal stress direction.

The role of stress gradients in identifying the length scale and critical fracture threshold associated with brittle fracture is investigated by comparing simulation results for the notched and the unnotched specimens. The simultaneous consideration of the notched and unnotched cases considerably narrows down the ranges of admissible material parameters associated with the Ritchie–Rice–Knott criterion.

The effect of temperature is investigated by isothermal analyses with various ambient temperatures. The model developed will be helpful to further analyze the effects of strain rate, specimen size, different notch and puncher head geometries, etc., on the transition temperature. Owing to its multi-axiality and loading history, the small punch test is most sensitive as a model validation tool which is why the present application of a numerical modeling scheme to small punch testing constitutes a novel approach.

## 2. Theory

### 2.1. Hypoelastic–plastic Model

Let  $\mathbf{X}$  and  $\mathbf{x}:=\boldsymbol{\phi}(\mathbf{X}, t)$  denote the particle positions in the reference (undeformed) configuration  $\mathcal{B}_0$  and current (deformed) configuration  $\mathcal{B}$ , respectively.<sup>1</sup>  $\mathbf{F}:=\partial\mathbf{x}/\partial\mathbf{X}$  defines the deformation gradient of the nonlinear motion map  $\boldsymbol{\phi} : \mathcal{B}_0 \times \mathbb{R}^{\geq 0} \rightarrow \mathbb{R}^3$ . Let  $\mathbf{l}:=\dot{\mathbf{F}} \cdot \mathbf{F}^{-1} = \partial\mathbf{x}/\partial\mathbf{x}$  denote the spatial velocity gradient, with  $\mathbf{v} = \dot{\mathbf{x}}$ . Splitting  $\mathbf{l}$  into its symmetric  $\mathbf{d}:=\text{sym}(\mathbf{l})$  and skewsymmetric  $\mathbf{w}:=\text{skw}(\mathbf{l})$  parts via  $\mathbf{l} = \mathbf{d} + \mathbf{w}$  where  $\mathbf{d}$  denotes the rate of deformation tensor we postulate the following additive decomposition of  $\mathbf{d}$

$$\mathbf{d} = \mathbf{d}_e + \mathbf{d}_p + \mathbf{d}_\theta, \quad (1)$$

with  $\mathbf{d}_e$ ,  $\mathbf{d}_p$  and  $\mathbf{d}_\theta$  representing its elastic, plastic and thermal parts, respectively. This forms the basis of hypoelastic–plastic formulations which rely on certain objective rates of the selected stress measures. We use the Green–Naghdi–McInnis rate of the Cauchy (true) stresses which requires the rotationally neutralized rate of the deformation tensor  $\hat{\mathbf{e}}$  defined as

$$\hat{\mathbf{e}} = \mathbf{R}^\top \cdot [\mathbf{d}_e + \mathbf{d}_p + \mathbf{d}_\theta] \cdot \mathbf{R} = \hat{\mathbf{e}}_e + \hat{\mathbf{e}}_p + \hat{\mathbf{e}}_\theta, \quad (2)$$

with  $\hat{\mathbf{e}}_e := \mathbf{R}^\top \cdot \mathbf{d}_e \cdot \mathbf{R}$ ,  $\hat{\mathbf{e}}_p := \mathbf{R}^\top \cdot \mathbf{d}_p \cdot \mathbf{R}$  and  $\hat{\mathbf{e}}_\theta := \mathbf{R}^\top \cdot \mathbf{d}_\theta \cdot \mathbf{R} = \mathbf{d}_\theta$ . Here,  $\mathbf{R}$  denotes the rotation tensor, carried out by the polar decomposition of the deformation gradient  $\mathbf{F} = \mathbf{R} \cdot \mathbf{U}$ , with  $\mathbf{U}$  representing the symmetric right stretch tensor. Similarly, a pull back operation on the Cauchy stress tensor  $\boldsymbol{\sigma}$  with the rotation tensor gives its rotationally neutralized counterpart:  $\hat{\boldsymbol{\sigma}} := \mathbf{R}^\top \cdot \boldsymbol{\sigma} \cdot \mathbf{R}$ . Its material time derivative  $\dot{\hat{\boldsymbol{\sigma}}}$  can be objectively integrated. Using the thermo-elastic constitutive relations one has

$$\dot{\hat{\boldsymbol{\sigma}}} = \mathbb{C}_e : \left[ \hat{\mathbf{e}} - \hat{\mathbf{e}}_p - \hat{\mathbf{e}}_\theta \right] = \mathbb{C}_e : \hat{\mathbf{e}}_e, \quad (3)$$

where  $\mathbb{C}_e$  denotes the elastic constitutive tensor with, for isotropic materials,

$$\mathbb{C}_e := \frac{\nu E}{[1+\nu][1-2\nu]} [\mathbf{1} \otimes \mathbf{1}] + \frac{E}{2[1+\nu]} [\mathbf{1} \oplus \mathbf{1} + \mathbf{1} \ominus \mathbf{1}]. \quad (4)$$

$E$  and  $\nu$  denote Young's modulus and Poisson's ratio, respectively. Moreover,

$$\dot{\hat{\mathbf{e}}}_\theta = \mathbf{d}_\theta = \alpha_\theta \dot{\Theta} \mathbf{1} \quad (5)$$

where  $\alpha_\theta$  denotes the thermal expansion coefficient and  $\Theta$  the temperature.

### 2.2. Model for ductile fracture – Gurson's porous plasticity – local formulation

The ductile fracture mode by progressive cavitation of a porous solid with a void volume fraction  $f$  is based on Gurson's dilatant plasticity model [11]. The model is extended by parameters  $q_1$ ,  $q_2$  and  $q_3$  in [12,13] to achieve better agreement with numerical analyses of unit cells, and by the bilinear function  $f^*(f)$  in [14] to account for rapid void coalescence prior to failure. The hydrostatic

<sup>1</sup> The following notations will be used. Consistently assuming  $\mathbf{a}$ ,  $\mathbf{b}$ , and  $\mathbf{c}$  as three second order tensors, together with Einstein's summation convention on repeated indices,  $\mathbf{c} = \mathbf{a} \cdot \mathbf{b}$  represents the single contraction product with  $c_{ik} = a_{ij}b_{jk}$ .  $d = \mathbf{a} : \mathbf{b} = a_{ij}b_{ij}$  represents the double contraction product, where  $d$  is a scalar.  $\mathbb{E} = \mathbf{a} \otimes \mathbf{b}$ ,  $\mathbb{F} = \mathbf{a} \oplus \mathbf{b}$ , and  $\mathbb{G} = \mathbf{a} \ominus \mathbf{b}$  represent the tensor products with  $E_{ijkl} = a_{ij}b_{kl}$ ,  $F_{ijkl} = a_{ik}b_{jl}$ , and  $G_{ijkl} = a_{ij}b_{jk}$ , where  $\mathbb{E}$ ,  $\mathbb{F}$ , and  $\mathbb{G}$  represent fourth order tensors.  $\partial_{\mathbf{a}}\mathbf{b}$  denotes  $\partial\mathbf{b}/\partial\mathbf{a}$ .  $\text{dev}(\mathbf{a}) = \mathbf{a} - 1/3 \text{tr}(\mathbf{a})\mathbf{1}$  and  $\text{tr}(\mathbf{a}) = a_{ii}$  stand for the deviatoric part of  $\mathbf{a}$  and trace of  $\mathbf{a}$ , respectively, with  $\mathbf{1}$  denoting the identity tensor.  $\text{sym}(\mathbf{a})$  and  $\text{skw}(\mathbf{a})$  denote symmetric and skew-symmetric portions of  $\mathbf{a}$  respectively.  $\dot{\mathbf{a}}$  gives the material time derivative of  $\mathbf{a}$ .  $\hat{\mathbf{a}}$  gives  $\mathbf{a}$  represented at the rotationally neutralized, i.e., corotational, configuration. Finally,  $\text{div}$  and  $\text{grad}$  denote the divergence and gradient operators with respect to the spatial configuration, respectively.

stress dependent flow potential  $\Phi_p$  is then formulated as

$$\Phi_p = \left[ \frac{\sigma_{eq}}{\sigma_y} \right]^2 + 2q_1 f^* \cosh\left(\frac{3q_2 \sigma_m}{2\sigma_y}\right) - [1 + q_3 f^{*2}] \leq 0. \quad (6)$$

$\sigma_{eq} = [3/2 \text{dev}(\hat{\sigma}) : \text{dev}(\hat{\sigma})]^{1/2}$  is the equivalent von Mises stress,  $\sigma_m = \text{tr}(\hat{\sigma})/3$  is the hydrostatic stress and  $q_1$ ,  $q_2$  and  $q_3$  are material parameters.<sup>2</sup> When  $f_c$  denotes the critical void volume fraction at incipient coalescence,  $f_f$  the fraction at failure and the material parameter  $f_u^* = 1/q_1$ , the bilinear function  $f^*(f)$  is defined as<sup>3</sup>

$$f^*(f) = \begin{cases} f & f \leq f_c, \\ f_c + [f_u^* - f_c] [f - f_c] / [f_f - f_c] & f > f_c. \end{cases} \quad (7)$$

The thermo-visco-plastic hardening of the material matrix is described by the flow stress  $\sigma_y$  which accounts for strain, strain rate and temperature dependences. Hence, letting  $e_p$  denote the equivalent plastic strain and  $\dot{e}_p$  its rate, we assume a Johnson–Cook type multiplicative form

$$\sigma_y(e_p, \dot{e}_p, \Theta) = h_y(e_p) r_y(\dot{e}_p) t_y(\Theta), \quad (8)$$

where  $h_y$ ,  $r_y$  and  $t_y$  denote the functions of strain hardening, strain rate hardening and thermal softening which are defined as

$$\begin{aligned} h_y(e_p) &= \sigma_{y0} + B e_p^n, \\ r_y(\dot{e}_p) &= 1 + C \log(\dot{e}_p / \dot{e}_{p0}), \\ t_y(\Theta) &= 1 - \Omega^m, \end{aligned} \quad (9)$$

where  $\sigma_{y0}$  is the initial yield stress (cf. Eq. (32)). The strain hardening is controlled by  $B$  and  $n$ , whereas strain rate and temperature dependence of hardening are controlled by  $C$  and  $m$ , respectively. The reference strain rate is denoted by  $\dot{e}_{p0}$ .

$$\Omega = [\Theta - \Theta_{ref}] / [\Theta_{melt} - \Theta_{ref}] \quad (10)$$

is the homologous temperature with  $\Theta_{ref}$  and  $\Theta_{melt}$  representing the reference and the melting temperatures, respectively.

Using the normality postulate, the plastic part of the rate of deformation tensor at the rotationally neutralized configuration is defined as

$$\hat{\epsilon}_p = \dot{\gamma} \partial_{\hat{\sigma}} \Phi_p, \quad (11)$$

which is not traceless due to the hydrostatic stress dependence of  $\Phi_p$ . Here,  $\dot{\gamma}$  denotes the plastic multiplier.<sup>4</sup>

According to the plastic work equivalence  $[1-f] \sigma_y \dot{e}_p = \hat{\sigma} : \hat{\epsilon}_p$ , the equivalent plastic strain rate reads

$$\dot{e}_p = \hat{\sigma} : \frac{\hat{\epsilon}_p}{[1-f] \sigma_y}. \quad (12)$$

The kinetic evolution of the void volume fraction involves nucleation and growth taking place during fully developed plastic flow. The time rate of change of the total void volume fraction is formulated additively in terms of void nucleation rate  $\dot{f}_n$  and void growth rate  $\dot{f}_g$

$$\dot{f} = \dot{f}_n + \dot{f}_g. \quad (13)$$

Assuming a strain dependent void nucleation [16],  $\dot{f}_n$  is written as

$$\dot{f}_n = A_N \dot{e}_p \quad \text{where} \quad A_N = A_N(e_p) = \frac{f_N}{S_N \sqrt{2\pi}} \exp\left(-\frac{[e_p - e_{pN}]^2}{2S_N^2}\right). \quad (14)$$

<sup>2</sup> The plastic potential reduces to that of Gurson's original proposal for  $q_1 = q_2 = q_3 = 1$ , and to that of von Mises isochoric plasticity for  $q_1 = q_3 = 0$ .

<sup>3</sup> As  $f \rightarrow f_f$ ,  $f^* \rightarrow f_u^*$  and the material loses its load carrying capacity which defines ductile fracture.

<sup>4</sup> The eventual framework is a consistency type rather than an over-stress type, see, e.g., [15]. That is, the computation of the plastic multiplier  $\dot{\gamma}$  exploits the consistency condition viz.  $\dot{\Phi}_p = 0$ .

In Eq. (14),  $e_{pN}$  and  $S_N$  denote the mean equivalent plastic strain at the incipient nucleation and its standard deviation, respectively.  $f_N$  denotes the total source of nucleation for the void volume fraction.

Following [9], we further split  $\dot{f}_g$  into

$$\dot{f}_g = \dot{f}_g^{\text{normal}} + \dot{f}_g^{\text{shear}} \quad (15)$$

with  $\dot{f}_g^{\text{normal}}$  accounting for the void growth under hydrostatic stresses and reflecting mass conservation:

$$\dot{f}_g^{\text{normal}} = [1-f] \text{tr} \hat{\epsilon}_p. \quad (16)$$

$\dot{f}_g^{\text{normal}}$  alone falls short to predict fracture modes under low stress triaxiality ratios; see, e.g., experimental studies reported in [17,18]. Hence,  $\dot{f}_g^{\text{shear}}$  is introduced to account qualitatively for the softening effects associated with void distortion, void interaction and with material rotation under shear stress states, see, e.g. [9]:

$$\dot{f}_g^{\text{shear}} = k_w f w(\text{dev} \hat{\sigma}) \frac{\dot{\epsilon}^p : \text{dev} \hat{\sigma}}{\sigma_{eq}} \quad (17)$$

where  $k_w$  is a material parameter with a suggested interval  $0 \leq k_w \leq 3$  [9] and  $0 \leq w \leq 1$  is the function which distinguishes the states of axisymmetric stress from those of generalized shear, i.e., pure shear plus a hydrostatic stress:

$$w(\text{dev} \hat{\sigma}) = - \left[ \frac{27 J_3}{2 \sigma_{eq}^3} \right]^2. \quad (18)$$

$J_3 = 1/3 [\sigma_{ij} - \sigma_m] [\sigma_{jk} - \sigma_m] [\sigma_{ki} - \sigma_m]$  is the third invariant of the deviatoric stress tensor. Note that  $w=0$  through  $J_3=0$  for all axisymmetric stress states, whereas  $w=1$  for the states of generalized shear.

Finally, in the absence of elastic–plastic heating related to latent elastic and inelastic structural changes or any heat source the temperature increase is due to the heat flux  $\mathbf{q}$  and plastic dissipation including void nucleation and growth

$$\rho c_p \dot{\Theta} = -\text{div} \mathbf{q} + \chi \hat{\sigma} : \hat{\epsilon}_p. \quad (19)$$

$\rho$  and  $c_p$  denote the density in the current configuration and the specific heat capacity. Fourier's law is assumed,  $\mathbf{q} = -k \text{grad} \Theta$ , with  $k$  denoting the thermal conductivity.  $\chi$  is the so-called Taylor–Quinney coefficient denoting the fraction of plastic work converted to heat [19].

### 2.2.1. Integral-type nonlocal regularization

Numerical solutions for the local material models accounting for softening lose uniqueness and suffer from a pathological dependence on the applied discretization. Hence, a consistent regularization requires incorporation of a material length scale which controls the width of localization in the numerical solutions, as demonstrated by, e.g., [20].

The present analysis uses the nonlocal integral type<sup>5</sup> regularization scheme presented in [22,23], see also, e.g., [24,25]. Let  $\dot{f}(\mathbf{x})$  represent the local damage rate at point  $\mathbf{x}$  defined at the current configuration. Its delocalization produces  $\dot{f}_{\text{nonlocal}}$  at  $\mathbf{x}$  according to

$$\dot{f}_{\text{nonlocal}}(\mathbf{x}) = \int_V \tilde{\omega}_{\text{ductile}}(\mathbf{x}, \mathbf{y}) \dot{f}(\mathbf{y}) dV(\mathbf{y}), \quad (20)$$

where  $\mathbf{y}$  represents the location vector at current coordinates and  $V$  the volume at the current configuration. Let  $\omega_{\text{ductile}}(\mathbf{x}, \mathbf{y})$  denote

<sup>5</sup> A gradient enhanced nonlocal formulation together with a Gurson-type plastic potential is used in, e.g., [21].

the bell shaped nonlocal weight function:

$$\omega_{\text{ductile}}(\mathbf{x}, \mathbf{y}) = \begin{cases} \left[1 - |\mathbf{x} - \mathbf{y}|^2 / R_{\text{ductile}}^2\right]^2 & \text{if } R_{\text{ductile}} \geq |\mathbf{x} - \mathbf{y}| \geq 0, \\ 0 & \text{if } R_{\text{ductile}} < |\mathbf{x} - \mathbf{y}|. \end{cases} \quad (21)$$

Here  $R_{\text{ductile}}$  denotes the ductile interaction radius, a parameter proportional to the material characteristic length associated with ductile fracture. The normalized weight function reads

$$\tilde{\omega}_{\text{ductile}}(\mathbf{x}, \mathbf{y}) = \frac{\omega_{\text{ductile}}(\mathbf{x}, \mathbf{y})}{\int_V \omega_{\text{ductile}}(\mathbf{x}, \mathbf{y}) dV(\mathbf{y})}. \quad (22)$$

With  $\tilde{\omega}(\mathbf{x}, \mathbf{y})$  any inconsistency pertaining to unrestricted averaging domains extending over the problem boundary is remedied. As long as boundaries are not violated,  $\int_V \omega_{\text{ductile}}(\mathbf{x}, \mathbf{y}) dV(\mathbf{y})$  is a constant. The local formulation is recovered for  $R_{\text{ductile}} \rightarrow 0$ , while for finite  $R_{\text{ductile}}$  the nonlocal formulation makes a difference in the presence of spatial gradients in the ductile damage variable.

### 2.3. Model for brittle fracture: the Ritchie–Knott–Rice maximum stress criterion

There exist numerous approaches for modeling cleavage in metallic materials. Based on the Weibull weakest link theory, Beremin's statistical model reflects random nature of brittle fracture and incorporates the effect of plastic flow, see, e.g., [26,27] or more recently [28]. The so-called energy limiters, which, by enforcing saturation in the strain energy function automatically bound stresses in the constitutive equations, constitute another approach to brittle fracture [29]. Continuum damage mechanics models, within a thermodynamics of internal variables formalism, introduce scalar or tensorial damage variables and their conjugate variables which allows not only modeling of stiffness and strength degradation associated with brittle (as well as ductile) damage but also determination of associated inelastic dissipation, see, e.g., [30]. Recently, in order to model the brittle fracture phase in ductile–brittle fracture transition the authors proposed a blend of continuum damage mechanics and Gurson's plasticity [31]. For additional recent developments in brittle fracture modeling and ductile–brittle fracture transition, we refer to, e.g., [32–34], among others. In the current study, following [1] and aiming at deterministic modeling of crack paths, we are using the simple yet powerful Ritchie–Knott–Rice criterion for modeling brittle fracture [10].

Let  $\sigma_1(\mathbf{x})$  represent the local maximum principal stress at point  $\mathbf{x}$  defined at the current configuration. Its delocalization reads

$$\sigma_{1,\text{nonlocal}}(\mathbf{x}) = \int_V \tilde{\omega}_{\text{brittle}}(\mathbf{x}, \mathbf{y}) \sigma_1(\mathbf{y}) dV(\mathbf{y}), \quad (23)$$

where  $\omega_{\text{brittle}}(\mathbf{x}, \mathbf{y})$  denotes the following nonlocal weight function:

$$\omega_{\text{brittle}}(\mathbf{x}, \mathbf{y}) = \begin{cases} 1 & \text{if } R_{\text{brittle}} \geq |\mathbf{x} - \mathbf{y}| \geq 0, \\ 0 & \text{if } R_{\text{brittle}} < |\mathbf{x} - \mathbf{y}|. \end{cases} \quad (24)$$

Here  $R_{\text{brittle}}$  denotes the brittle interaction radius, defining characteristic length associated with brittle fracture. The normalized weight function reads

$$\tilde{\omega}_{\text{brittle}}(\mathbf{x}, \mathbf{y}) = \frac{\omega_{\text{brittle}}(\mathbf{x}, \mathbf{y})}{\int_V \omega_{\text{brittle}}(\mathbf{x}, \mathbf{y}) dV(\mathbf{y})}. \quad (25)$$

According to the RKR criterion [10] once  $\sigma_{1,\text{nonlocal}}(\mathbf{x})$  reaches a critical value  $\sigma_c$ , brittle fracture results. The criterion can be formulated as

$$\sigma_{1,\text{nonlocal}} = \sigma_c. \quad (26)$$

Following [1],  $\sigma_c$  is independent of temperature and strain rate.  $R_{\text{brittle}}$  is linked to the size of the cleavage grain  $V_{\text{cleavage}}$ . Hence, the interaction radius of brittle fracture is larger than that of

**Table 1**  
Chemical composition of P91 in wt%.

C	Si	Mn	P	S	Cr	Mo	V	Ni	Nb	N
0.10	0.27	0.53	0.007	0.01	8.76	0.91	0.2	0.35	0.04	0.038

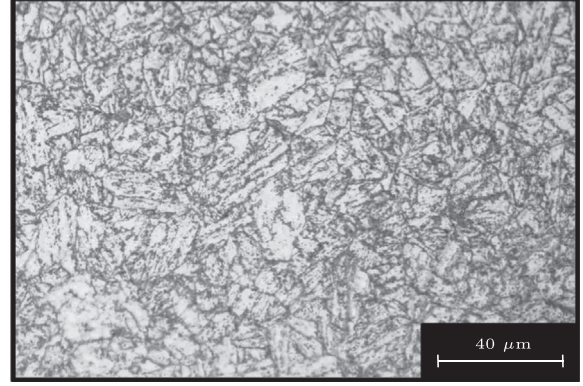


**Fig. 1.** Optical micrograph showing the tempered martensitic structure of P91 steel.

intragranular ductile fracture. One should note that the RKR criterion does not require plastic flow. By being non-cumulative, it is different from the nonlocal treatment of Gurson's model, as each integration associated with the time step is independent.

## 3. Experiments

In small punch fracture tests a non-deformable hemispherical puncher loads a rigidly clamped disk-shaped specimen at constant displacement rate deforming it through an aperture in the lower die. The specimen design recommended in the Code of Practice is a disk with diameter  $d=8$  mm and thickness 0.5 mm [8]. During the test, the puncher force and the central disk deflection (or puncher displacement) are recorded. Small punch force-deflection (or displacement) curves are then used to estimate mechanical properties such as yield stress, ultimate tensile strength and ductile–brittle transition temperature.

### 3.1. Chemical composition and microstructure observation of P91 steel

In this study, a ferritic/martensitic P91 steel is used for small punch fracture tests over a wide temperature range. P91 is an advanced steel for high temperature applications, especially, in power plants where creep resistance is of importance. However, components may be exposed to loading at lower or intermediate temperatures as well. Thus, toughness and ductile–brittle transition temperature are important, particularly, if components are subjected to irradiation which deteriorates those properties. The chemical composition of the P91 steel is given in Table 1.

The prevailing microstructure of P91 consists of tempered martensite (as shown in the optical micrograph in Fig. 1) and secondary phases that precipitate on martensite lath, prior-austenite grain boundaries and in the ferrite matrix. Precipitates result from the tempering process which is applied to improve the ductility and toughness of the martensitic structure.  $M_{23}C_6$  (M denotes Cr, Fe, or Mo) carbides mainly precipitate on prior-austenite grain boundaries, martensite lath and delta-ferrite boundaries whereas smaller MX (M denotes V or Nb, and X is C or N) particles precipitate in the matrix [35].

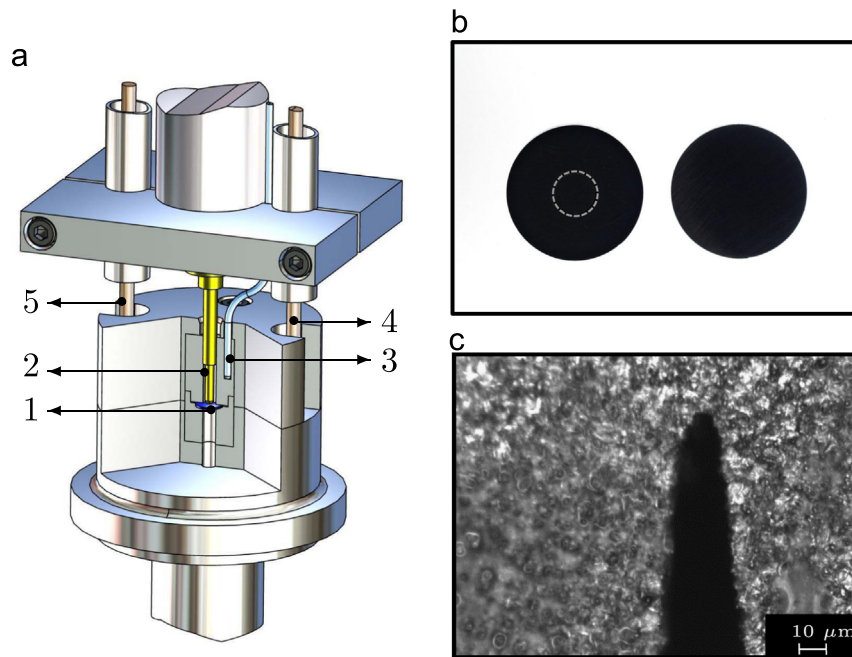


**Fig. 2.** Experimental equipment and specimens: (a) instrumented specimen holder of small punch fracture testing equipment (1: small punch disk, 2: hemispherical ended punch, 3: thermocouple, 4/5: LVDT); (b) small punch disks with a circular V notch (dotted circle represents the notch) and standard unnotched small punch disks; (c) cross-sectional view of notch tip.

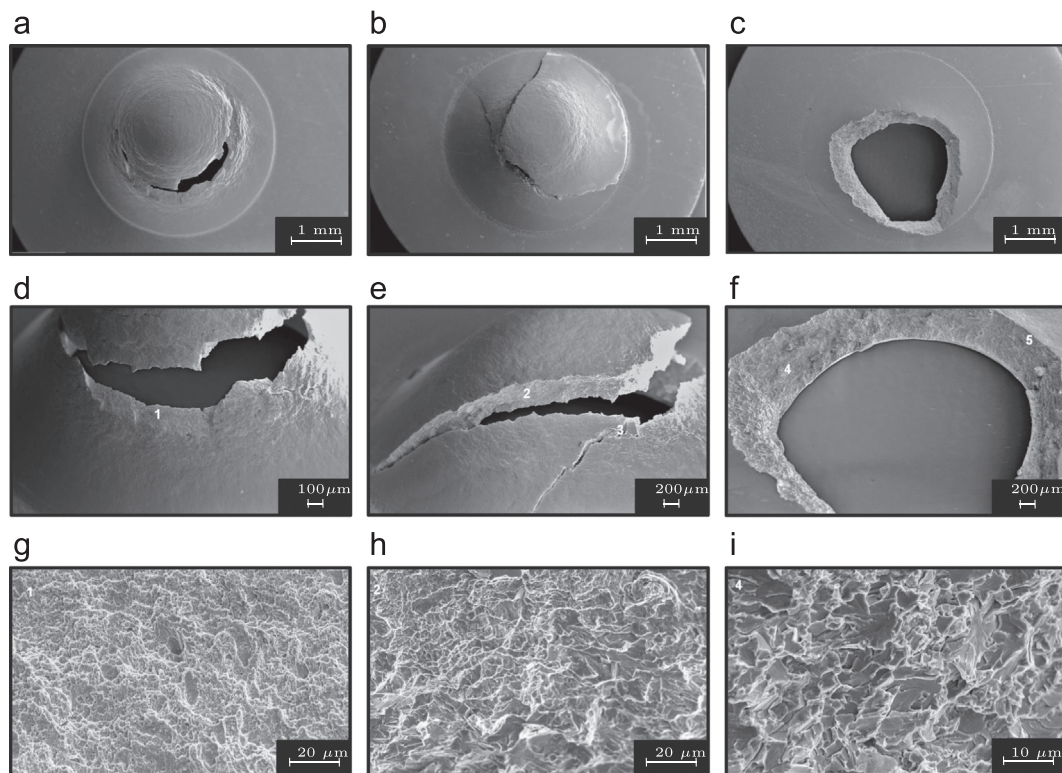


**Fig. 3.** Fracture appearance of failed unnotched small punch disks tested at different temperatures and the corresponding fracture surfaces: (a) 25 °C, ductile failure with (d) presenting a close view and (g) its fracture surface; (b) –158 °C, ductile to brittle transition region, with (e) presenting a close view and (h) its fracture surface; (c) –196 °C, brittle failure, with (f) presenting a close view and (i) its fracture surface.

### 3.2. Experimental setup

The small punch fracture tests were carried out according to the guidelines of the Code of Practice [8]. The specimen holder (see Fig. 2(a)) consists of upper and lower dies between which the specimens were clamped firmly. The receiving aperture of the

holder was 4 mm. The test rig was mounted in a universal testing machine equipped with an environmental chamber allowing temperature control from –150 °C to +300 °C. The actual temperature range was between –196 °C and 25 °C. To achieve the lowest test temperature –196 °C, the specimen holder was immersed in a vessel (not shown in Fig. 2(a)) filled with liquid

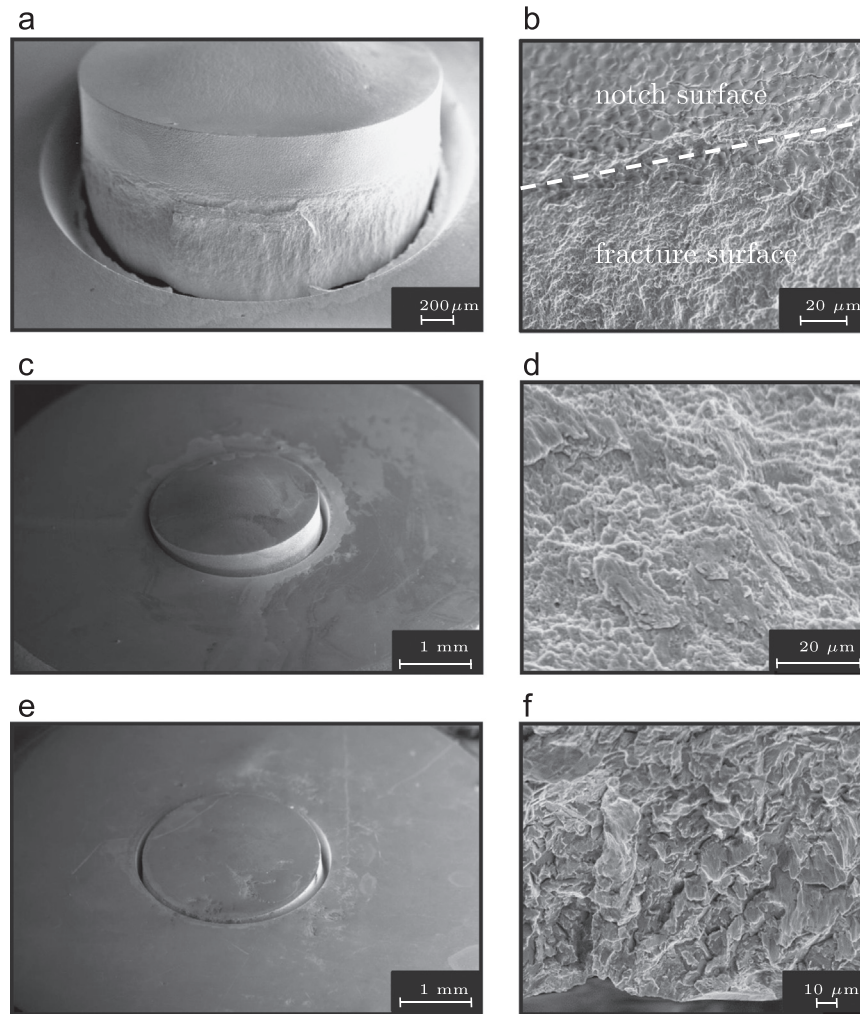


**Fig. 4.** Fracture appearance at the circular notch: small punch disks with notch depth of 0.5 mm tested at (a) 25 °C, (b) –158 °C and (c) –196 °C and the corresponding fracture surfaces given in (d), (e) and (f), respectively. For the disk tested at 25 °C dimples, and for the disk tested at –196 °C cleavage facets are visible.

nitrogen, while the environmental chamber remained idle. The temperature was measured by a Type T thermocouple with an accuracy of  $\pm 2$  °C. Before starting a test, sufficient time was given to the system to reach thermal equilibrium, as verified by pre-tests with an additional thermocouple spot-welded to a dummy specimen. Two Class 2 linear variable displacement transducers mounted to the puncher rod measured the puncher displacement. The small punch disks were deformed under a constant velocity of the cross-head of 0.005 mm/s.

For all small punch tests, disks of 8 mm diameter were used: unnotched disks with 0.5 mm nominal thickness and notched disks with 1 mm thickness. The circular V notches which were produced by electrical discharge machining had a diameter of 2.5 mm, a notch tip radius of approximately 5  $\mu\text{m}$  and different notch depths of 0.3, 0.4 and 0.5 mm (Fig. 2(b) and (c)).

### 3.3. Observations at macroscale

With decreasing temperature reduced bulging and increased cleavage facets (i.e., decreasing amount of plastic deformation until failure) are noted from the overall appearance of the unnotched small punch disks (Fig. 3(a)–(c)). Fig. 3(a)–(f) reveals the macroscopic crack patterns. At 25 °C, where the material fails in a ductile manner, the crack pattern is circular. This fracture appearance is valid approximately till –100 °C where the ductile–brittle transition regime starts. The crack initiates where necking

takes place on the bottom surface, propagates through the thickness and follows a circumferential path along this necking region (Fig. 3(a), (d), see also [36,6]). In the transition region (Fig. 3(b), (e), test temperature –158 °C) ductile and brittle features are observed to coexist. Radial cracks as indications of brittle behavior develop from the widely open semi-circular crack, see, e.g., [37,38]. At –196 °C, disks fail in an almost completely brittle mode with insignificant plastic deformation, exhibiting a more piecewise linear crack propagation path (Fig. 3(c), (f)).

### 3.4. Observations at microscale

The fracture mode at the upper shelf (from 25 °C down to approximately –100 °C) is completely ductile. The fracture surface features dimples and small microvoids (Fig. 3(g)) which are dominant in number and nucleated by fine MX precipitates. Less frequent larger voids are nucleated by coarser  $\text{Mo}_{23}\text{C}_6$  precipitates. In the transition region, both ductile and brittle fracture features consisting of transgranular cleavage facets co-exist (Fig. 3(h)). The amount of ductile crack growth gradually decreases with decreasing temperature. At the lowest test temperature, –196 °C, the fracture surfaces are almost completely brittle as depicted in Fig. 3(i).

Fig. 4 presents fractured notched disks tested at temperatures 25 °C, –158 °C and –196 °C. On the right, the corresponding fracture surfaces are given. For 25 °C, the surface is covered by microvoids. Ductile tearing ahead of the notch is revealed. For

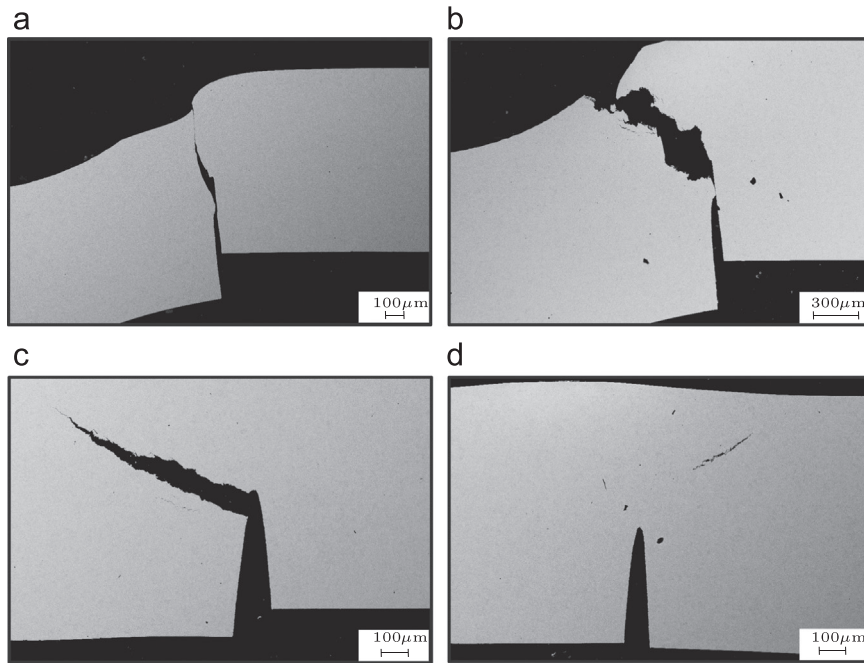


**Fig. 5.** SEM images of specimen sections of the notched small punch disks fractured at (a) 25 °C, (b) –158 °C and (c) –196 °C showing the crack propagation direction from the notch tip, as well as (d) arrested secondary cracks away from the notch tip at –196 °C [39].

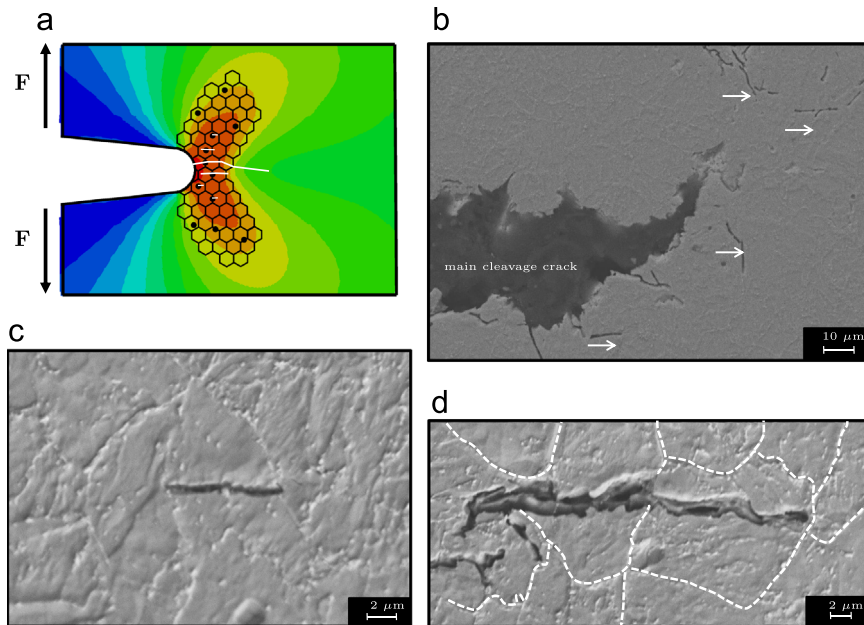


**Fig. 6.** Cleavage crack arrest: (a) scheme showing the arrest mechanisms; (b) SEM image showing main cleavage crack and secondary cracks in its vicinity (observations performed on a notched disk tested at –196 °C); (c) microcrack initiated at a precipitate inside the grain and arrested at grain boundaries; (d) higher magnification SEM image of a secondary crack arrested at a grain boundary and in the matrix (grain boundaries are highlighted).

–158 °C, the fracture surface is characteristic of quasi-cleavage with tear ridges here and there which are the source of plastic deformation noted for this temperature. To observe the fracture surface of the –196 °C specimen, the central bulged part was removed to get an SEM image of this zone. Cleavage facets confirmed the brittle fracture prevailing for this temperature.

### 3.5. Crack propagation direction

As stated in [39], the radial symmetry of the notch promotes a plane strain condition. Owing to the small radius of the notch tip,

high stress concentrations could be achieved so that the initiation of the crack was found to start from the notch tip.

SEM images of sections of small punch disks for different temperatures representative of the upper shelf, lower shelf and transition region were acquired to identify the crack propagation directions as given in Fig. 5. For the ductile case (where void initiation and growth are controlled by plastic strain), the crack propagation was found to follow the direction of the notch along the maximum equivalent plastic strain. At 25 °C, microvoids nucleated at MX and Mo<sub>23</sub>C<sub>6</sub> in the vicinity of the notch tip grow and coalesce as the strain level increases. Subsequently, a continuous crack is formed leading to complete fracture. At –196 °C,

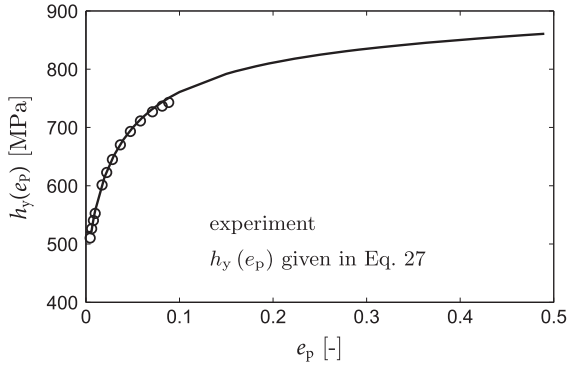


**Fig. 7.** Flow curve of P91 at room temperature. The circles represent experimentally recorded points prior to necking and the solid line is a plot of Eq. (27) for the parameters given.

microcracks form due to cracking of larger  $\text{Mo}_{23}\text{C}_6$  precipitates [40] in the highly stressed region close to the notch tip and propagate almost perpendicular to the maximum tensile stress. In the transition region both ductile and brittle fracture mechanisms compete, while the macrocrack follows an angle in between the ductile and brittle cases, closer to the brittle case.

Second phase particles which are responsible for void nucleation in ductile fracture mode act as microcrack initiators in the cleavage fracture mode. As schematically illustrated in Fig. 6(a), ahead of the stress concentration provided by the notch, cracking of brittle second phase particles can take place and microcracks can propagate in the matrix. Cracks may get arrested at grain boundaries or in neighboring grains, if the driving stress is not high enough. Fig. 6 illustrates possible scenarios. In Fig. 6(b) the secondary cracks around the main cleavage crack are visualized according to the sketch given in Fig. 6(a). If these cracks are observed under higher magnification, different mechanisms can be identified. In Fig. 6(c) a microcrack initiated from a secondary phase particle and got arrested in the same grain, whereas in (d) a microcrack is noted which propagated into the adjacent grains and got arrested at a grain boundary on one side, and in the matrix on the other side.

#### 4. Thermomechanical material parameters for P91 steel

Isotropy in both elasticity and plasticity is assumed<sup>6</sup> since the disks were extracted from thick-walled pipes without significant texture. A temperature dependent modulus of elasticity is assumed,  $E(\theta) = -0.1127\theta + 243.6$  in GPa with  $\theta$  in K (adapted from [41]). This corresponds to  $E=210$  GPa,  $E=230.6$  GPa and  $E=234.9$  GPa at 25 °C, –158 °C and –196 °C, respectively. Poisson's ratio is  $\nu=0.3$  for all temperatures. The thermal expansion coefficient is  $\alpha_\theta = 1.3 \times 10^{-5} \text{ K}^{-1}$ , the melting temperature and the reference temperature are  $\theta_{\text{melt}} = 1717$  K and  $\theta_{\text{ref}} = 298$  K, respectively. The specific heat capacity is  $c_p = 622 \text{ m}^2 \text{ K}^{-1} \text{ s}^{-2}$  according to data supplied by the producer. Finally, the Taylor–Quinney coefficient is taken as  $\chi=0.9$ .

The plastic hardening behavior is based on tensile tests conducted at constant engineering strain rate of  $5 \times 10^{-5} \text{ s}^{-1}$ . The data up to maximum tensile force, i.e., the necking point, is used. A simple power-law hardening in the Johnson–Cook form turned out insufficient. Thus, we adopted the following function (cf. Eqs. ((13) and (14)))

$$h_y(e_p) = \begin{cases} \sigma_{y0} + h_0 e_p & e_p \leq e_{p0} \\ h_1 e_p + \sigma_{y\infty} - [\sigma_{y\infty} - \sigma_{y1}] \exp(-m e_p^n) & e_p > e_{p0} \end{cases} \quad (27)$$

<sup>6</sup> For convenience, Table 3 compiles the material parameters listed in this section.

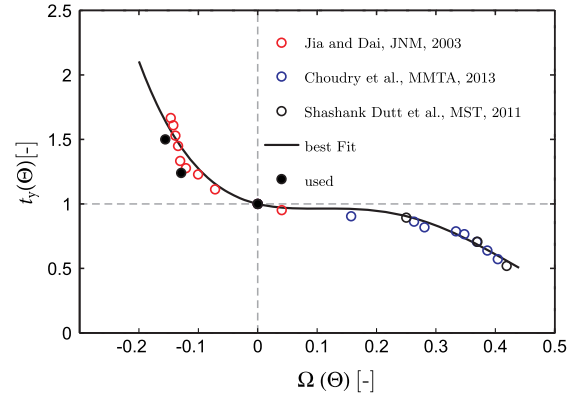


**Fig. 8.** Homologous temperature  $\Omega$  dependence of the yield stress scaling parameter  $t_y(\theta)$  after processing three experimental sources as an initial guess for parameter identification. Comparisons based on force–displacement response of simulations with experiments of small punch tests at 25 °C, –158 °C and –196 °C. Source 1 is the unirradiated T91 from Fig. 1 of [42], for temperatures smaller or slightly higher than room temperature. Source 2 is adopted from the true stress–true plastic strain data at various temperatures for 9Cr–1Mo steel tested at a strain rate of  $3.16 \times 10^{-4} \text{ s}^{-1}$  from Fig. 3 of [43] for temperatures equal or greater than room temperature. Finally, Source 3 represents data given in Table 1 of [44] which lists the tensile properties of P91 steel for temperatures equal or greater than room temperature.

where the associated parameters at room temperature have been identified as  $h_0 = 123$  MPa,  $h_1 = 75$  MPa,  $\sigma_{y0} = 520$  MPa,  $\sigma_{y1} = 376$  MPa,  $\sigma_{y\infty} = 831$  MPa,  $m=6.14$ ,  $n=0.541$  and  $e_{p0}^n = 0.006$ . The experimentally determined data and fitted flow curve are shown in Fig. 7.

The scaling factor  $t_y(\theta)$  controls the temperature dependence of the flow curve and is given in terms of homologous temperature in Fig. 8. Assessing the temperature dependence for a wide range of temperatures including cryogenic and elevated temperatures is not straightforward as, in the literature, either low or high temperatures are studied. In the current study, the temperature dependence of the flow curve was established by merging different results reported in the literature<sup>7</sup> and a best fit was used. It is seen that the distribution of the data required a function with an inflection point. Hence, the single curvature model of Johnson–Cook was not sufficient. The best fit was supplied by the fourth order polynomial,  $42.562\Omega^4 - 44.846\Omega^3 + 11.438\Omega^2 - 1.1021\Omega + 1$ , where  $\Omega = [\theta - \theta_{\text{ref}}] / [\theta_{\text{melt}} - \theta_{\text{ref}}]$ . The comparison of punch force–displacement simulations with the experiments at the three different temperatures (25 °C, –158 °C and –196 °C) required a slight deviation from the best fit of tensile data, and led us to  $t_y(\theta)$  equal to 1, 1.24 and 1.54 for 25 °C, –158 °C and –196 °C, respectively. The corresponding points are marked as “used” in Fig. 8. A rate dependence was not taken into account.

Following [12,13], the parameters of the extended Gurson model are chosen as  $q_1 = 1.5 = 1/f_u^*$ ,  $q_2 = 1$ ,  $q_3 = q_1^2 = 2.25$ . The initial void volume fraction<sup>8</sup> is selected as  $f_0 = 0.00044$ . The parameters associated with the nucleation mechanism  $f_N = 0.02$ ,  $\epsilon_N =$

<sup>7</sup> A non-dimensional ratio of the actual yield stress with respect to the one reported at room temperature (i.e., reference temperature of each study) is produced.

<sup>8</sup> Franklin's formula [45] serves as an estimate for the initial void volume fraction  $f_0$

$$f_0 = \frac{0.054 \sqrt{d_x d_y}}{d_z} \left[ S(\%) - \frac{0.001}{\text{Mn}(\%)} \right] \quad (28)$$

Here,  $d_x$ ,  $d_y$ , and  $d_z$  denote average inclusion diameters in the respective directions. S% and Mn% represent the weight percentages of sulphur and manganese in the matrix, respectively. For  $d_x = d_y = d_z$  and the chemical composition of P91 given in Table 1, we have  $f_0 = 0.00044$ . Although Franklin's formula is used for materials where manganese sulphide inclusions are the critical particles for fracture, it supplies a realistic initial value for porosity for the investigated material whose chemical content also involves S and Mn. Moreover, the authors' simulations on

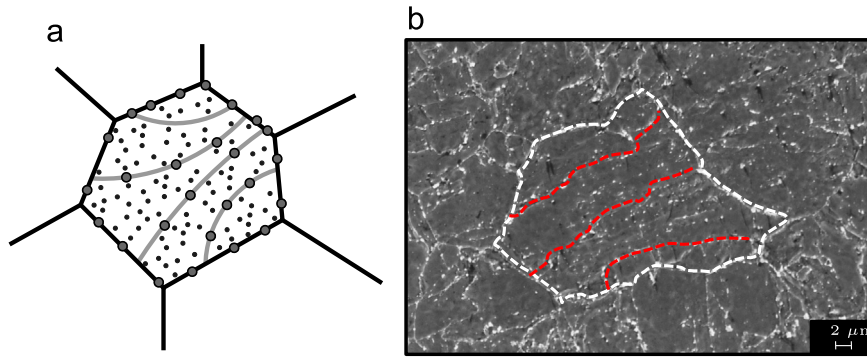


Fig. 9. (a) Scheme representing P91 microstructure, (b) SEM image of polished–etched sample revealing this structure.

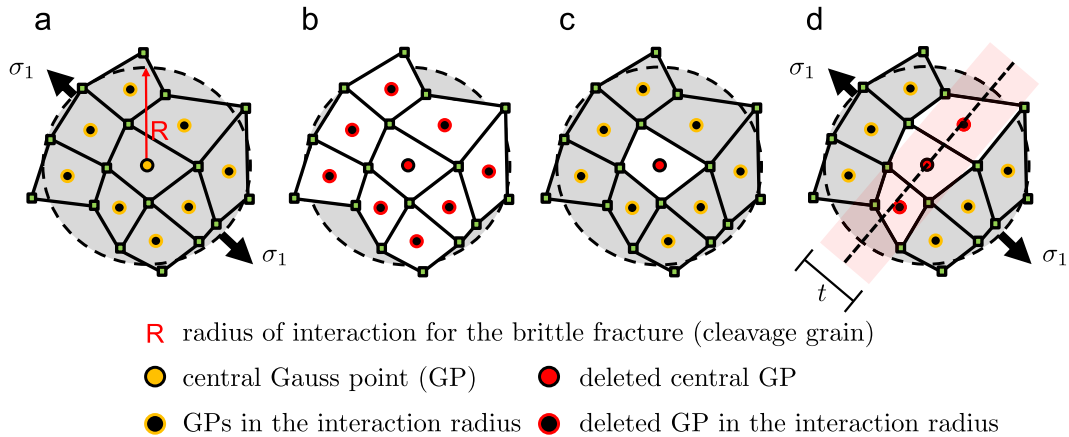


Fig. 10. Methods of virtual extension of cleavage cracks for the cleavage grain given in (a). (b) Deletion of the whole cleavage grain, e.g., [1]. In this method many elements are deleted without any directional information on the crack formation. (c) Deletion of central element only: only the central element is deleted once the criterion is satisfied. Again this method suffers from ignoring directional information for crack propagation. (d) Deletion of elements whose GPs fall into a band oriented in the direction orthogonal to the maximum tensile principal stress: Deletion band size  $t$  can be selected according to the finite element size. Hence,  $\mathbf{x}_c$  is the position vector of the central GP and  $\mathbf{x}$  is the position vector of the neighboring GP with respect to a common origin and  $\mathbf{n}$  is the unit vector in direction of the maximum principal stress (belonging to the central element), then deletion is applied to elements for which  $(\mathbf{x} - \mathbf{x}_c) \cdot \mathbf{n} \leq t/2$ . We observed that the fracture patterns for total deletion (b) and single deletion (c) resulted in fracture islands and largely deleted regions with considerable mass loss, respectively.

0.3 and  $S_N = 0.1$  are selected, following [46,47] suggesting that the volume fraction of the segregated inclusions  $f_N$  is within a narrow band of 0.01–0.03.

Our simulations of notched samples show that the notch induces a strong plane strain effect with  $w$  reaching 1 and increased triaxiality (Eq. (18)). This amplifies the effect of the shear modification. As a consequence, incorporation of the shear modification results in simulated crack initiation significantly preceding the experimentally observed one. Hence,  $k_w = 0$  is selected and the shear modification is suppressed for simplicity. By this choice the void nucleation rather than the void growth term incorporates the shear stress effects provided that hydrostatic stresses are positive. Regarding the uniqueness of the parameter choice, we note that it is also possible to arrive at reasonable fracture initiation strains with  $k_w \neq 0$  and relaxed void nucleation and/or initial porosity data.

For the final void fraction at failure, different references give somewhat different results, e.g., [48] takes  $f_F = 0.25$  in accordance with [49] whereas  $f_F = 0.2$  is used in [50,51,46,47], noting that the last two references study steel A533 B. In the present work coalescence and failure porosity were taken as  $f_c = 0.1$  and  $f_F = 0.25$ . The so-called energetic length scale for ductile fracture has been suggested to be between four times the void size and half the void

spacing, see [22]. If two populations of second phase particles are present, which is the case for P91, one should select the population which is dominant in crack initiation and propagation. In our fractographic images, fine dimples initiated by small MX particles are noticeable. This precipitate type prevails in quantity and is believed to play a significant role in the ductile fracture (Fig. 3(g)) in addition to  $M_{23}C_6$  precipitates. From the images the relevant length scale being of the order of the average distance between the MX and the  $M_{23}C_6$  precipitates was identified as 2.5–5  $\mu\text{m}$  and used to define the lower and upper bounds of  $R_{\text{ductile}}$ , respectively. These values pose restrictions in selecting the finite element mesh size which scales the computational cost. One could also use a local formulation where the mesh size constitutes the characteristic length. This was not pursued in the current study due to the need to vary the mesh size around the notch tip as well as the relatively large aspect ratio of the elements in this region.

According to the RKR cleavage model, cracks initiate if a critical stress is exceeded over a characteristic distance, associated with the grain size. As previously mentioned, P91 microstructure is composed of prior austenite grains which are subdivided into packets of fine martensite laths (Fig. 9(a)). In order to reveal the microstructure and make prior austenite grain boundaries distinguishable, Vilelas reagent (1 g picric acid and 5 mL HCl in 100 mL ethanol) was used for etching. In Fig. 9(b) an SEM image of an etched sample is given. The two types of precipitates  $M_{23}C_6$  (with M identified as Mo by EDX analysis) and MX are apparent in this image:  $M_{23}C_6$  mostly in the prior austenite subgrain boundaries whereas MX distributed in the matrix. The grain size

(footnote continued)

unnotched disks show that initial porosity estimates within (0.0044, 0.002) resulted in only marginal differences in the computed failure times.

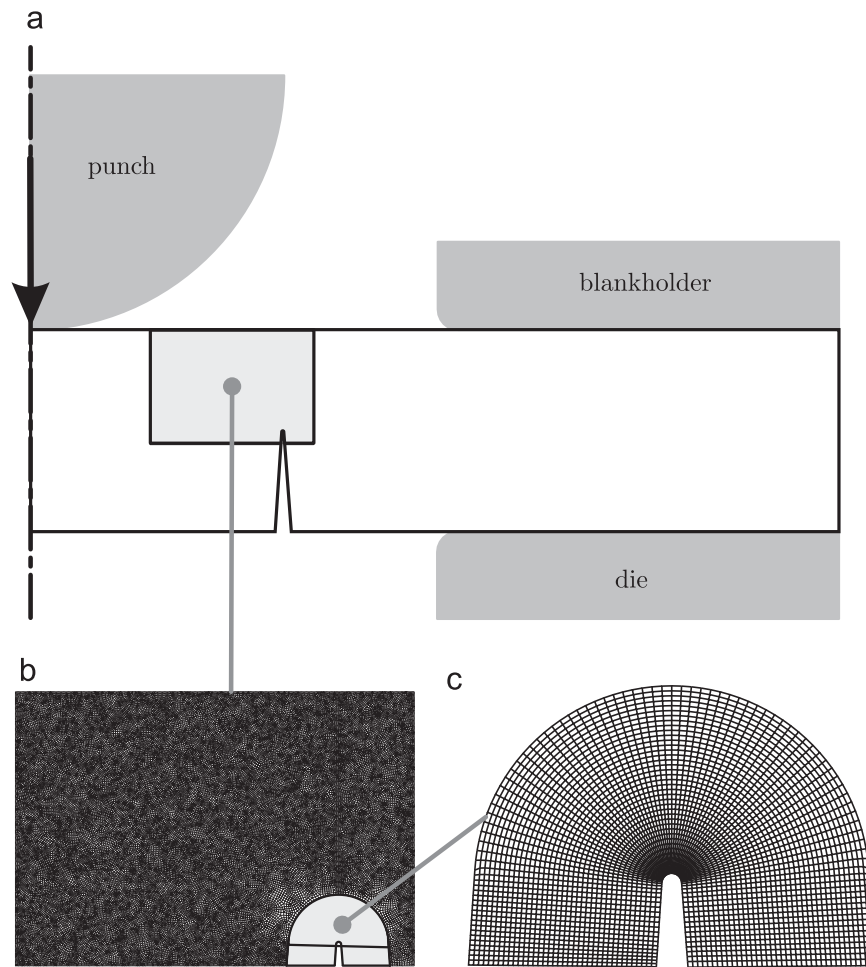


**Fig. 11.** (a) Axisymmetric finite element model for the notched small punch test. In (b) and (c) the mesh design is depicted where the region in (c) corresponds to the ALE remeshing region.

determined by the intercept method (ASTM E112) was found to be 14–25  $\mu\text{m}$  which is comparable with values reported in the literature. This was used to define lower and upper bounds of  $R_{\text{brittle}}$  as 7  $\mu\text{m}$  and 12.5  $\mu\text{m}$ . For the associated critical stress for brittle fracture, the present numerical computations suggested  $\sigma_c = 2.83\sigma_{y0}$  and  $\sigma_c = 2.55\sigma_{y0}$ . The latter yielded reasonable results if small-scale yielding conditions prevail. For unnotched small punch specimens, however, the former gave better results as large-scale yielding conditions have to be taken into account. No temperature dependence of  $\sigma_c$  was assumed.

## 5. Simulations

2D axi-symmetric simulations with CAX4R reduced integration elements for temperatures of  $-196^\circ\text{C}$ ,  $-158^\circ\text{C}$  and  $25^\circ\text{C}$  were conducted in ABAQUS/EXPLICIT with double precision. The dies and the punch were modeled as rigid bodies and the disk as a deformable body. The interaction between the rigid and deformable bodies was assumed to be constant with a temperature independent friction coefficient chosen as  $\mu = 0.25$ . A solution of quasi-static problems with a dynamic-explicit solution procedure generally involves a large number of time steps due to the Courant stability condition. In order to reduce the computational cost, mass scaling was applied with a target time step of  $10^{-3}$  s over the whole analysis which lasted 150 s. This supplies acceleration of the simulations without changing the actual time scale of the process affecting other time dependent phenomena such as viscosity or heat transfer.

The heat source is localized at the crack tip. However, since the loading rate is low, this concentration is effectively lost by diffusion, without significant effect on the material response. This is the case for ductile fracture with relatively low propagation rate as well as brittle fracture with high propagation rate but limited plastic flow and accompanying dissipation. Therefore, we use an isothermal analysis for the three different temperatures.

Crack propagation was modeled using an element erosion technique whereby elements with Gauss points whose porosity and/or normalized RKR integral reach the corresponding failure thresholds are removed from the computational stack. Doing so within a nonlocal environment is possible in different ways as depicted in Fig. 10 for brittle fracture. Without loss of generality, the same scenarios apply for ductile fracture as well. The first method consists in deleting the whole element set within the interaction radius once the central element's Gauss point becomes critical (ductile or brittle failure threshold reached), e.g., [1]. If the internal length associated with the failure mechanism is large, this can result in a violation of mass conservation. Alternatively, only the central element can be deleted. For virtually ductile crack extension we applied this method and eroded only the single central element. For brittle fracture with a larger material length scale, however, our studies showed that this method results in cleavage crack islands formed by eroded elements ahead of the crack tip. These crack islands can be seen as computational counterparts of arrested cracks around the crack tip, as found experimentally, which are then bridged either by ductile or brittle fracturing. Although simple, this method does not allow any control on the crack propagation direction. However, it is well known that the principal stress is

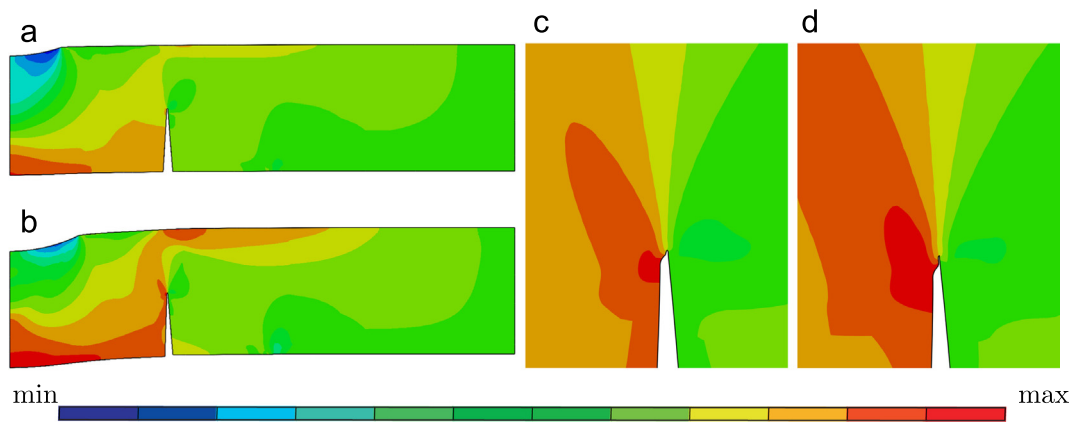


**Fig. 12.** RKR integral distribution (normalized with respect to  $\sigma_{y0}$ ) at four stages of loading at  $-196$  °C. (a) Punch displacement  $u = 0.088$  mm, [max 2.075; min  $-3.185$ ]; (b) punch displacement  $u = 0.187$  mm, [max 2.324; min  $-2.664$ ]; (c) punch displacement  $u = 0.187$  mm, detail at notch, [max 2.324; min  $-2.664$ ]; (d) punch displacement  $u = 0.23$  mm, [max 2.535; min  $-2.739$ ]. At punch displacement  $u = 0.187$  mm the maximum occurs at the notch rather than the bottom for the first time.

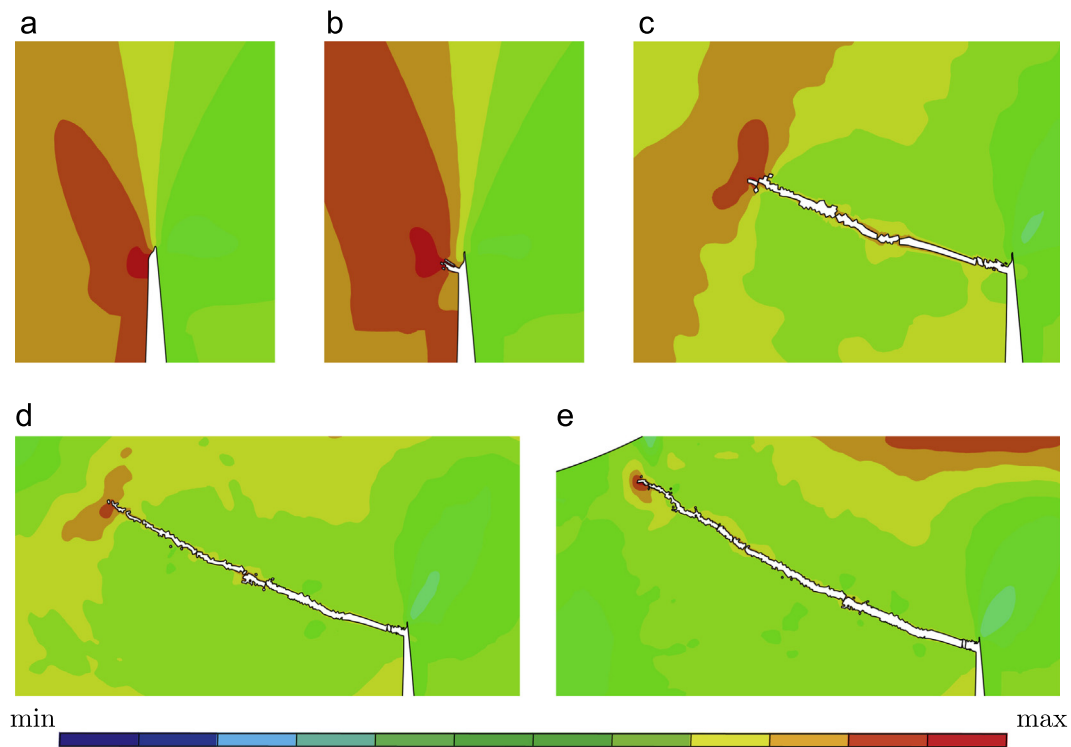


**Fig. 13.** Initiation and evolution of the crack at different stages of loading at  $-196$  °C. RKR integral distribution (normalized with respect to  $\sigma_{y0}$ ) at five different successive loading steps: (a)  $u = 0.230$  mm [max 2.535; min  $-2.739$ ]; (b)  $u = 0.231$  mm [max 2.359; min  $-2.731$ ]; (c)  $u = 0.232$  mm [max 2.269; min  $-2.757$ ]; (d)  $u = 0.233$  mm [max 2.251; min  $-2.508$ ]; (e)  $u = 0.234$  mm [max 2.351; min  $-1.420$ ].

effective in directing cleavage cracks. Thus, a new method was implemented: once the central element's normalized RKR integral reached the corresponding failure threshold the element itself, as well as the elements whose Gauss points fell within a crack band thickness along the direction orthogonal to the maximum tensile principal stress, were deleted all together.

### 5.1. Small scale yielding condition

This set of simulations concerns the notched small punch tests where the fracture, either ductile or brittle, emanates from the notch as a result of stress concentration. We use the upper limits of the brittle and ductile interaction radii where  $R_{\text{ductile}} = 5 \mu\text{m}$  and  $R_{\text{brittle}} = 12.5 \mu\text{m}$  with  $\sigma_c = 2.55\sigma_{y0}$ .

The mesh used in the simulations is given in Fig. 11. Due to high stress gradients around the notch tip the finite element discretization

requires special attention in that region. In the current study  $2 \mu\text{m}$  mesh size allowed traversing the notch tip with sufficiently fine mesh for a reasonable notch tip stress resolution.<sup>9</sup> This requires the application of a nonlocal theory, since the emerging element sizes are smaller than the interaction radius identified for ductile failure. Since the radius of interaction is  $5 \mu\text{m}$  the utilized finite element sizes should be smaller than this to allow delocalization to be applied. Consequently, with the utilized mesh up to 230 elements in the

<sup>9</sup> As noted in [27,1], for sufficiently smooth stress gradients the finite element size can be adapted to the grain size in order to circumvent an integration over a number of elements. However, for small-scale yielding conditions where a sharp notch or crack tip creates high stress gradients or for materials involving secondary microstructural mechanisms acting at a smaller scale, the maximum finite element sizes are limited by that smaller scale.

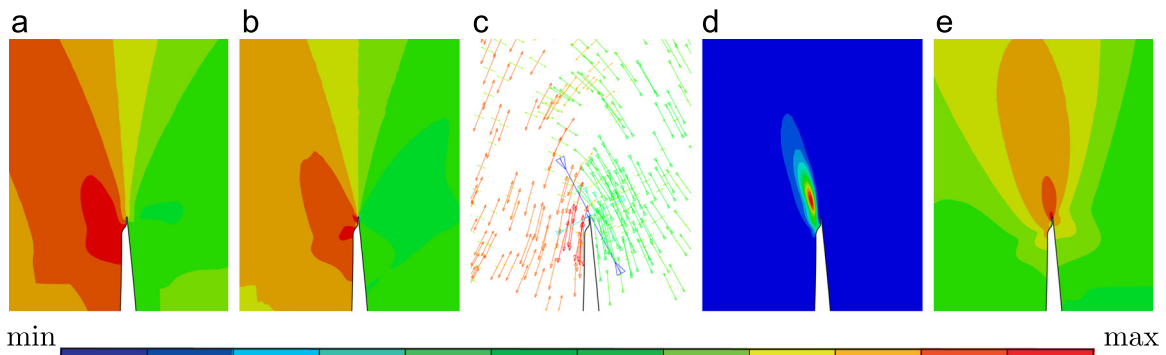


**Fig. 14.** Different field distributions at punch displacement  $u = 0.23$  mm for  $-196$  °C. (a) RKR integral distribution [max 2.535; min  $-2.739$ ]; (b) maximum normalized principal stress distribution [max 3.086; min  $-4.056$ ]; (c) in-plane principal stresses with associated directions [max = 1605 MPa; min =  $-3631$  MPa]; (d) total void volume fraction [max = 0.013; min =  $3.679 \times 10^{-7}$ ]; (e) von Mises equivalent stress [max = 1498 MPa; min = 17.74 MPa].

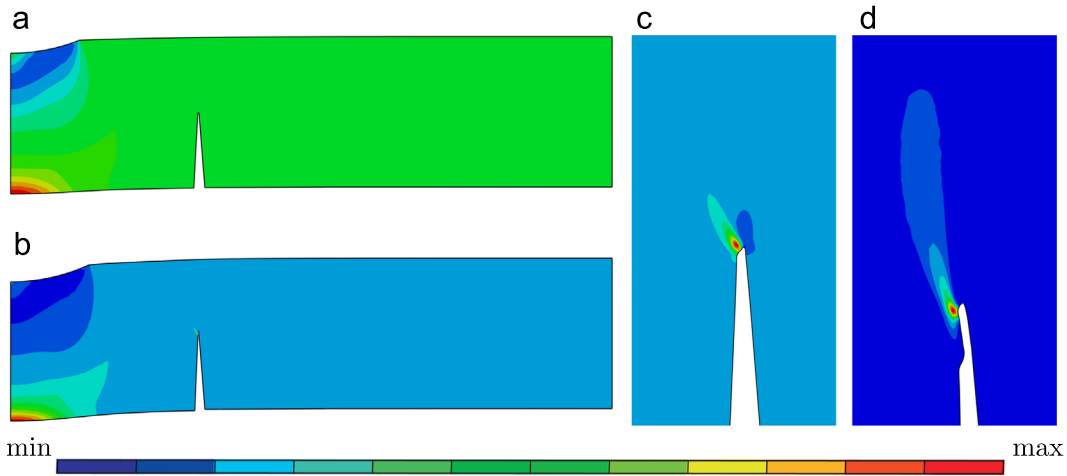


**Fig. 15.** Void volume fraction distribution at four different stages of loading at 25 °C. (a) Punch displacement  $u = 0.11$  mm, [max  $9.294 \times 10^{-4}$ ]; (b) punch displacement  $u = 0.157$  mm, [max  $2.162 \times 10^{-3}$ ]; (c) punch displacement  $u = 0.157$  mm, detail at notch, [max  $2.162 \times 10^{-3}$ ]; (d) punch displacement  $u = 0.405$  mm, [max 0.2186]. At punch displacement  $u = 0.157$  mm the void density concentrates for the first time at the notch rather than the bottom. The minimum porosity is set to zero in all these contour plots.

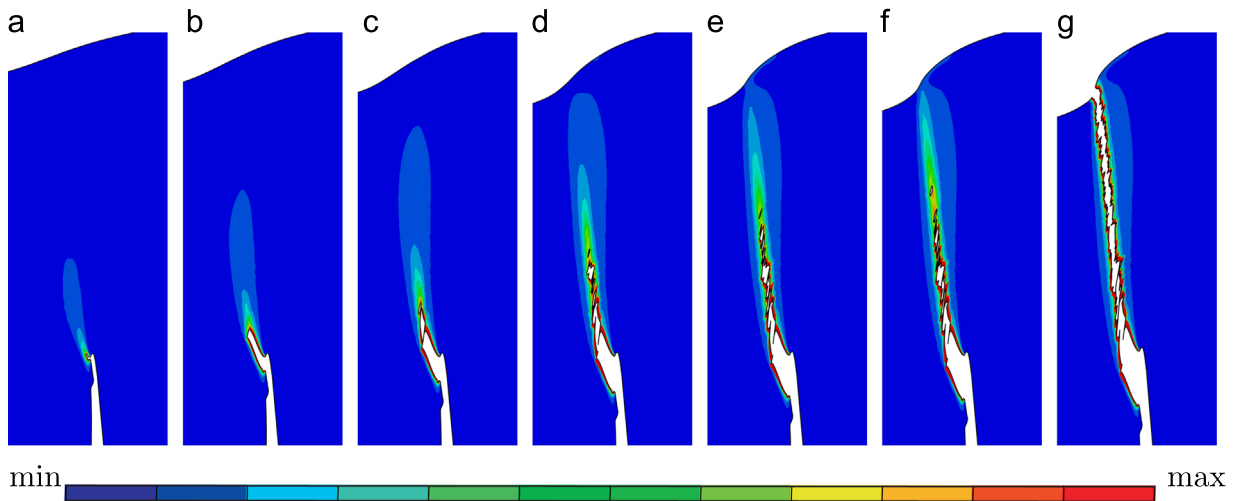


**Fig. 16.** Initiation and evolution of the crack at different stages of loading at 25 °C evidenced by contours of void volume fraction. Maximum void volume fraction is naturally 0.25 and minimum is set to zero.

vicinity and around 40 elements further away from the notch is supplied within a brittle interaction radius.

At the notch tip the Arbitrary Lagrangian Eulerian (ALE) remeshing<sup>10</sup> was utilized where VDISP subroutine interface allowed us

(footnote continued)

creation of a new mesh, and solution variable remapping with advection process. In order to preclude accumulation of numerical errors associated with solution mapping and delocalization operations and also keeping the computational cost to a reasonable limit, the number of ALE remeshing increments is kept minimum through a trial and error analyses. Accordingly the selected parameters are as follows: ALE remeshing frequency: 50 (typically 5–100 without Eulerian boundaries), remeshing sweeps per increment: 1 (default), Initial remeshing sweeps: default.

<sup>10</sup> ALE adaptive remeshing is used to remedy excessive distortion of the elements in the mesh at the notch vicinity. It consists of two fundamental steps:

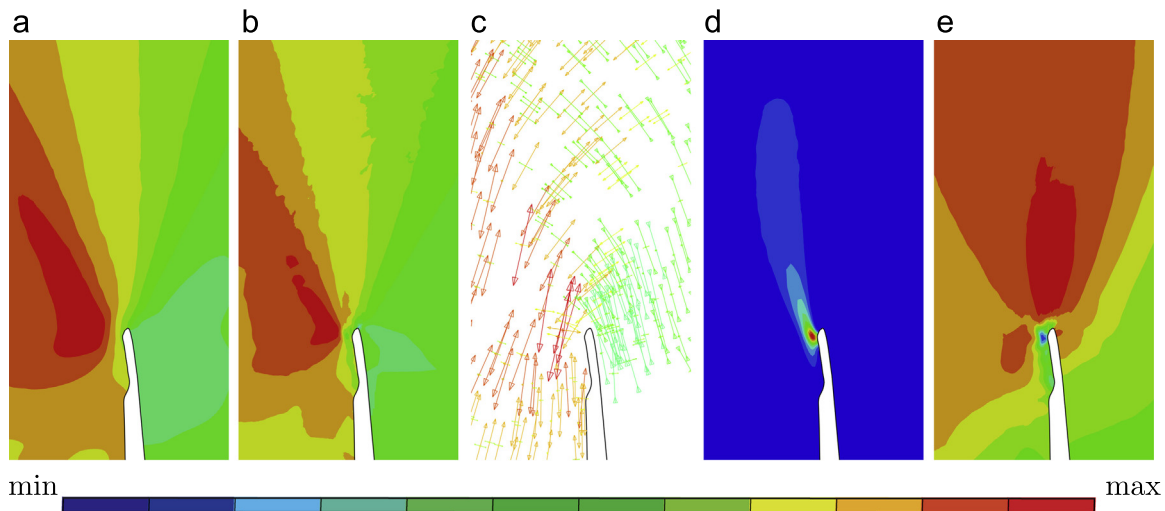


**Fig. 17.** Field distributions at punch displacement  $u = 0.405$  mm for  $25$  °C. (a) RKR integral [max 2.271; min  $-1.719$ ]; (b) maximum normalized principal stress [max 2.551; min  $-2.242$ ]; (c) in-plane principal stresses with associated directions [max=1362 MPa; min =  $-2320$  MPa]; (d) total void volume fraction [max=0.0219; min =  $6.830 \times 10^{-5}$ ]; (e) von Mises equivalent stress [max=926.6 MPa, min = 22.42 MPa].

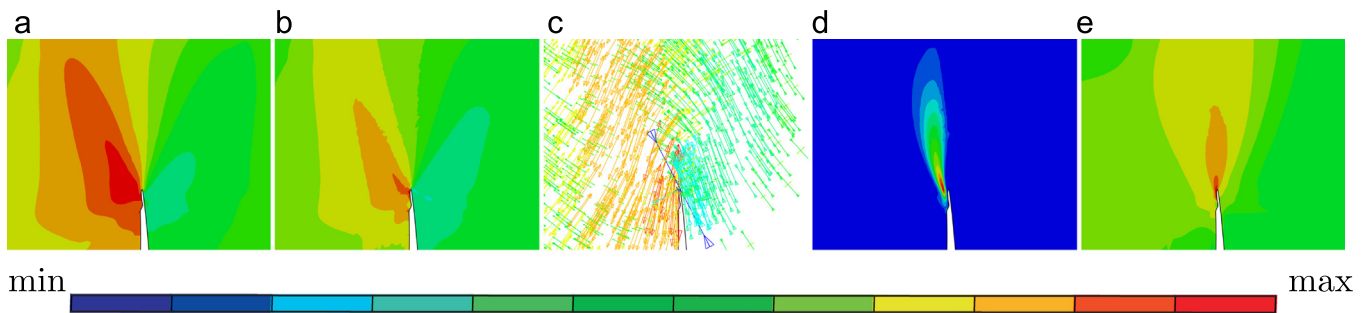


**Fig. 18.** Field distributions at punch displacement  $u = 0.36$  mm for  $-158$  °C. (a) RKR integral [max 2.518; min  $-1.940$ ]; (b) maximum normalized principal stress [max 3.395; min  $-2.324$ ]; (c) in plane principal stresses with associated directions [max=1789 MPa; min =  $-2412$  MPa]; (d) total void volume fraction [max=0.0406; min =  $3.934 \times 10^{-5}$ ]; (e) von Mises equivalent stress [max=1370 MPa, min = 22.97 MPa].

to track the corresponding element volumes. By morphing the mesh compatible with the underlying deformation this avoids otherwise extreme element distortion or aspect ratio change around the notch tip for the ductile fracture. Hence, smooth distributions of stress and strain fields are obtained which is conclusive in the damage development. Apart from the notch tip the mesh was created by the advancing front quad method. The number of elements within the effective radius of each element varied spatially. The size of the ALE region was determined by a trial and error analysis. Possible self-contact of the notch free surface was taken into account.

For  $-196$  °C, the main fracture mechanism is cleavage controlled by the stress over the cleavage grain. In order to shed light on the mechanism, we investigated the distribution of the Ritchie–Rice–Knott (RKR) integral normalized by  $\sigma_{y0}$  for various stages of loading (Fig. 12).

In early stages of the process, the RKR integral has its maximum first on the symmetry axis on the convex surface of the bent region, say the tip of the dome, whose magnitude is far from critical. With further loading, the critical region is carried away from the center but still stays on the free surface. At a punch displacement of  $u = 0.187$  mm till the crack initiation the maximum RKR integral is found on the left-hand side of the notch tip where hydrostatic stress is tensile. Taking into account the interaction radius for brittle

fracture the visibility criterion (Fig. 25) gives a reasonable distribution of the RKR integral over the region at the notch tip. Without visibility criterion the sign change of the maximum principal stresses at either side of the notch results in smaller values of the RKR integral at the fracture region around the notch. This unrealistic smoothing affects the threshold value for the RKR integral to be used. Situations with the maximum RKR integral being at the bottom of the disk can then occur at the instant of experimentally determined brittle fracture. Hence, the implementation of the visibility criterion seems to be crucial for the current application, where the interaction radius is larger than the notch radius.

The cleavage crack starts at the notch root where the RKR integral first reaches the threshold (Fig. 13). Fast cleavage crack propagation follows until the complete separation and loss of load carrying capacity of the disk. Throughout the loading, the RKR integral maintains the direction of the crack, while its maximum remains at the advancing crack tip. The crack propagation is not completely straight but slightly bent due to the redistribution of stresses induced by the continuous motion of the punch. This is in agreement with experimental findings, and it shows that the virtual crack propagation methodology is correctly taking into account the slight rotation of the maximum stress direction ahead of the advancing crack.

Fig. 14 shows the distribution of various fields around the notch tip just before the initiation of brittle fracture at punch displacement  $u = 0.23$  mm. From (a) to (e), the fields are the normalized RKR integral, the normalized maximum principal stress, the vector distribution of the maximum and minimum principal stresses, the

(footnote continued)

The remaining ALE adaptive mesh controls are selected as the default values proposed, see, e.g., [52].

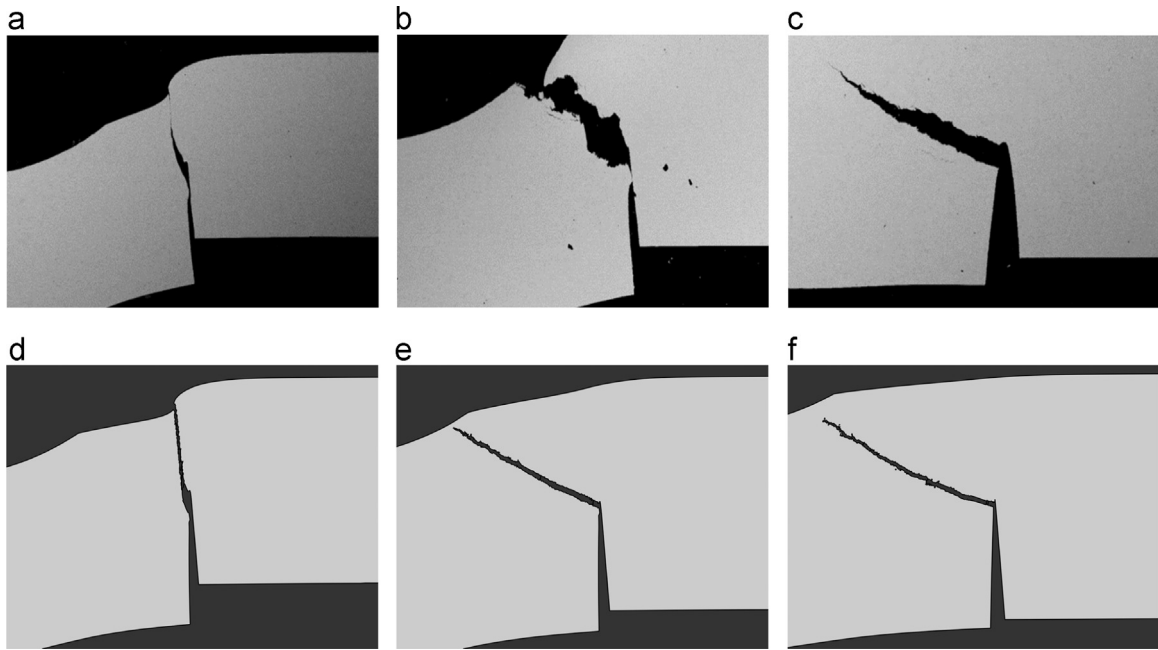


**Fig. 19.** Comparison of the crack patterns observed in simulations and experiments. (a) Experiment at 25 °C (simulation given in (d)); (b) experiment at -158 °C (simulation given in (e)); (c) experiment at -196 °C (simulation given in (f)).

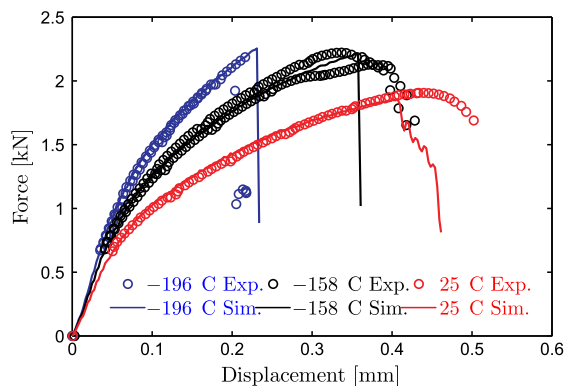


**Fig. 20.** Comparison of experimental and numerical punch force–displacement plots, with two repeat tests at the lower shelf (-196 °C) and the transition region temperature (-158 °C).

total void volume fraction and the von Mises stress, respectively. The RKR integral considerably smoothens the high gradients of the underlying principal stress field. As anticipated, the directions of the maximum (tensile) principal stress define the direction orthogonal to the crack propagation. Thus, fracture is of Mode I. The dominantly compressive (right) and tensile (left) stress fields separated by the notch are also apparent. The maximum void volume fraction, unlike the RKR integral, is located ahead of the notch tip which coincides with the given distribution of the von Mises stress. However, at this stage of loading its magnitude is far from being critical, in line with the brittle nature of fracture at -196 °C.

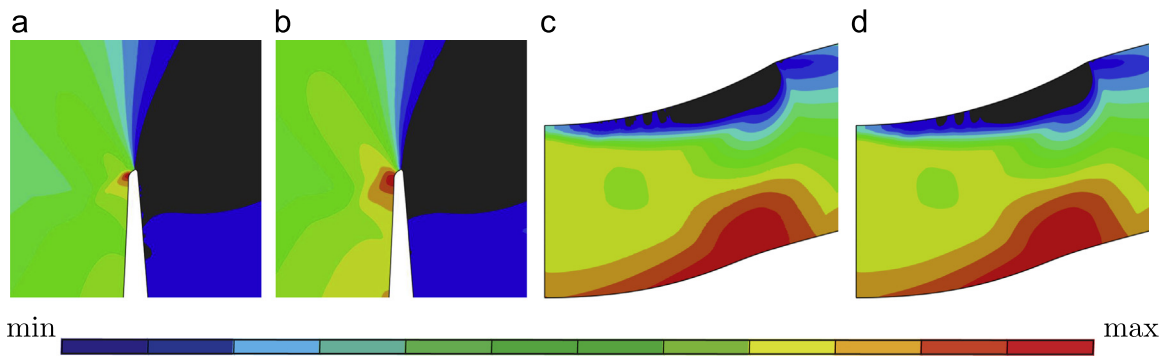
For 25 °C, ductile fracture is mainly controlled by plastic flow and hydrostatic stress with focus now being on the distribution of the void volume fraction at various stages of loading (Fig. 15). In the early stages of the process the void volume fraction has its maximum on the symmetry axis at the apex of the bend, however, with a magnitude far from the failure threshold. After a punch displacement of  $u = 0.157$  mm till the incipient fracture, the maximum porosity is located ahead of the notch tip, however, slightly shifted to the left where the hydrostatic stress is tensile. As the punch travel continues its magnitude and extension gets

larger, while the porosity growth tends to align itself along the punch loading direction.

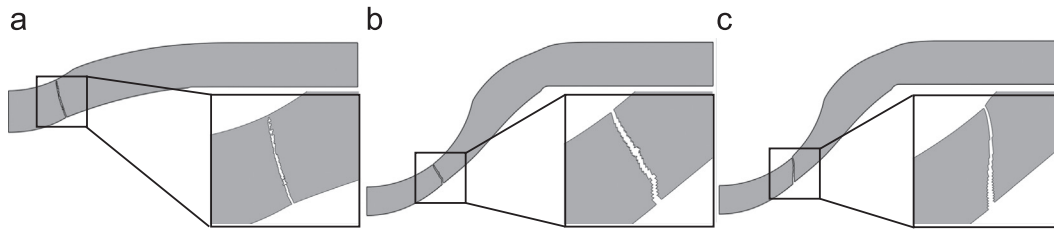
Fig. 16 shows the crack propagation from its initiation to complete separation. In accordance with the distribution of the porosity, the crack propagates almost parallel to the punch loading direction after a slight inflection to the left at the initial stage. This pattern is in good agreement with experimental findings. The whole process is governed by ductile failure, in the sense that the element deletion proceeds according to the ductile fracture criterion. The speed of crack propagation is considerably lower than in the brittle case. The failure process is distributed over a longer time period with larger energy required. The initiation and propagation of the crack feature mixing of Mode I and Mode II, noting that during almost vertical propagation Mode II dominates.

Fig. 17 displays various fields around the notch tip just before the initiation of ductile fracture at punch displacement  $u = 0.405$  mm: normalized RKR integral, the normalized maximum principal stress, the vector distribution of the maximum and minimum principal stresses, the total void volume fraction and the von Mises stress, from (a) to (e), respectively. The normalized RKR integral is considerably smaller than the threshold. Similar to the findings for -196 °C it deviates from the normalized maximum principal stress due to the high stress gradients at the notch tip. The principal stress vectors are similar in direction to the ones for -196 °C, however, with considerably reduced magnitudes. The temperature dependence of the yield stress causes plastic flow to take place at lower stress levels than for -196 °C. Without brittle fracture intervening, the notch tip experiences sufficient deformation to accumulate a critical amount of porosity under tensile hydrostatic stresses. Moreover, the von Mises equivalent stress (as driving force for the plastic deformation) has its maximum ahead of the crack tip and the contours orient themselves along the vertical direction of punch travel.

For -158 °C, fracture initiates at an intermediate punch travel  $u = 0.23$  mm, however, with a brittle mode. Fig. 18 displays the fields around the notch tip just before fracture initiation. While the accumulated porosity is higher than for -196 °C prior to fracture, it still remains below the coalescence void volume fraction. Thus, ductile fracture does not take place. The accumulation of sufficiently



**Fig. 21.** Effect of gradients on nonlocal averaging for  $-196\text{ }^{\circ}\text{C}$  and interaction radius of  $7\text{ }\mu\text{m}$ . (a) Notched model, before delocalization, maximum normalized principal stress distribution [max 2.742; min 0]; (b) notched model, after del., normalized RKR integral distribution [max 2.278; min 0]; (c) unnotched model, before del., maximum normalized principal stress distribution [max 2.744; min 0]; (d) unnotched model, after del., normalized RKR integral distribution [max 2.742; min 0].



**Fig. 22.** Crack patterns for the unnotched disk test simulations. (a)  $-196\text{ }^{\circ}\text{C}$ , (b)  $-158\text{ }^{\circ}\text{C}$  and (c)  $25\text{ }^{\circ}\text{C}$ .

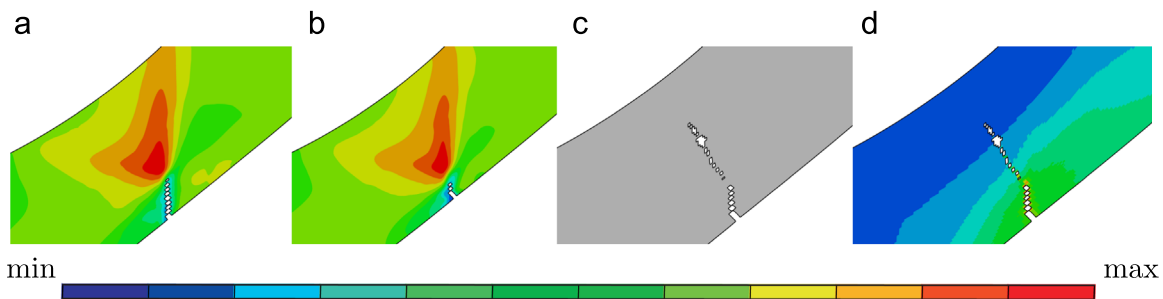


**Fig. 23.** (a) Normalized RKR integral distribution at  $25\text{ }^{\circ}\text{C}$  [max 2.294; min 0]; (b) the same for  $-158\text{ }^{\circ}\text{C}$  [max 2.784; min 0]; (c) transition from ductile to brittle fracture; (d) corresponding void volume fraction far below threshold.

high stress levels requires more deformation though. Consequently, hardening takes place at the crack tip.

A comparison of the crack patterns observed in simulations and experiments is given in Fig. 19. Obviously, the crack patterns for both  $25\text{ }^{\circ}\text{C}$  and  $-196\text{ }^{\circ}\text{C}$  are in very good agreement. For  $25\text{ }^{\circ}\text{C}$ , besides the crack pattern itself, the similarity of the upper face curvatures of the disk is noteworthy. For  $-196\text{ }^{\circ}\text{C}$ , although the direction of the crack is well reproduced, axisymmetry conditions are not preserved during brittle fracture in the experiments. For  $-158\text{ }^{\circ}\text{C}$  the fracture takes place much later than for  $-196\text{ }^{\circ}\text{C}$ . The fracture mode is predominantly brittle in the simulations, while the experimental findings show more mixing of ductile and brittle fracture. Also, it is seen that the steepness of the propagation direction decreases with decreasing temperature. For  $-158\text{ }^{\circ}\text{C}$ , the orientation of the crack lies in between those of  $25\text{ }^{\circ}\text{C}$  and  $-196\text{ }^{\circ}\text{C}$ .

Finally, a comparison of the punch force vs. displacement curves is given in Fig. 20. A good agreement is observed throughout the elastic–plastic deformation phase. At  $-196\text{ }^{\circ}\text{C}$ , the fracture strains are also well captured. For  $25\text{ }^{\circ}\text{C}$ , a slightly premature failure is obtained with a rather steep drop of the force response. For  $-158\text{ }^{\circ}\text{C}$ , although the displacement at fracture is close to the experimental ones, a more brittle mode of fracture results in a steeper drop of the force response compared to the experimental findings. This discrepancy is supposed to be emphasized by the fact that the axisymmetric 2D simulations cannot capture the distributed failure of the specimen along the circular notch as observed in 3D.

Small punch deformation energies up to fracture are obtained by integrating the total area under the load–displacement curves. According to the Code of Practice [8], a small punch disk is defined to fail when a 20% load drop after maximum load is reached. If deformation energies are plotted as a function of temperature, a sigmoidal increase is revealed similar to an impact energy vs. temperature graph of Charpy tests. For the experiments average deformation energies for  $-196\text{ }^{\circ}\text{C}$ ,  $-158\text{ }^{\circ}\text{C}$  and  $25\text{ }^{\circ}\text{C}$  are calculated to be 292 Nmm, 678 Nmm and 703 Nmm, respectively. For the simulations these are 340 Nmm, 549 Nmm and 619 Nmm, respectively. Hence, quantitatively the energy requirements until brittle or ductile fracture are well captured.

Simulations also allow quantification of the average crack tip speed during crack propagation. For  $-196\text{ }^{\circ}\text{C}$ ,  $-158\text{ }^{\circ}\text{C}$  and  $25\text{ }^{\circ}\text{C}$ , the average crack speeds turned out to be 1.42 mm/s, 1.06 mm/s and 0.037 mm/s, respectively, meaning that for  $-196\text{ }^{\circ}\text{C}$  the crack speed exceeded that of  $25\text{ }^{\circ}\text{C}$  by approximately a factor of 40. The closeness of  $-196\text{ }^{\circ}\text{C}$  and  $-158\text{ }^{\circ}\text{C}$  crack speeds also points at the predominately brittle nature of fracture at  $-158\text{ }^{\circ}\text{C}$ .

## 5.2. Small- and large-scale yielding conditions

The results in the previous section refer to small-scale yielding conditions, which work well for the notched specimens. Our unnotched specimen simulations with the same interaction radius of  $12.5\text{ }\mu\text{m}$  and  $\sigma_c = 2.55\sigma_{y0}$  governing brittle fracture, however,

showed premature fracturing, at about one fourth of the actual fracture displacement observed in the experiments. This is why we have a closer look at the role of this interaction radius.

For brittle interaction radii even larger than  $12.5 \mu\text{m}$ , the nonlocal operator causes increasing levelling of the notch tip RKR field such that the disk bottom exhibits the maximum RKR integral in excess of the one at the notch tip. Besides being out of the predefined bounds for the brittle interaction radius as set by the microstructural observations, the use of a larger interaction radius makes it impossible to obtain the correct location of brittle fracture at the notch tip at reasonable punch displacements.

On the other hand, interaction radii smaller than  $7 \mu\text{m}$  make the delocalized RKR integral get closer to the local. In the absence of stress concentrator in the unnotched case, the RKR integral cannot reach the threshold level, at least not at realistic strains as observed in the experiments. Hence, a set of values within the interval  $[7 \mu\text{m}, 12.5 \mu\text{m}]$  should be used. However, unlike the previous approach, where we first defined the length scale then the critical RKR threshold, the length be selected can be selected for the unnotched specimens after defining a critical fracture stress, because gradients are much less pronounced and, therefore, less affected by the selected length scale.

We found that  $R_{\text{brittle}} = 7.0 \mu\text{m}$  with  $\sigma_c = 2.83\sigma_{y0}$  gave acceptable results for both the notched and unnotched cases in so far as brittle fracture onset could be predicted reasonably well. One should note that interaction radii within  $[7 \mu\text{m}, 12.5 \mu\text{m}]$  did not affect the RKR integrals for the unnotched tests as much as for the notched ones. In order to be consistent with the previous analysis, the ductile fracture parameter was also reduced to its lower limit, i.e.,  $R_{\text{ductile}} = 2.5 \mu\text{m}$ . This corresponds to the smallest mesh size in the region with mesh refinement. Hence, at the notch tip the ductile damage delocalization applies for the finest elements. For the region away from the notch, fracture development is controlled by the mesh size, the smallest of which is equal to the

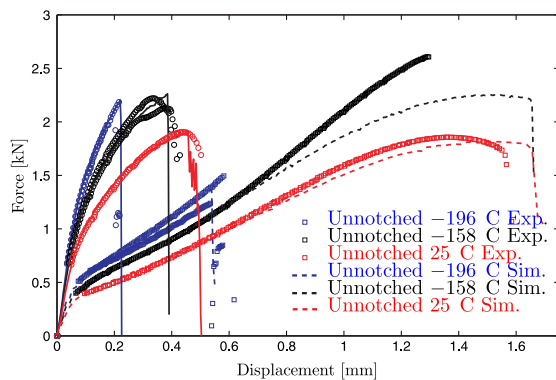


**Fig. 24.** Comparison of experimental and numerical punch force–displacement plots for notched and unnotched tests. The unmarked curves belong to the notched tests shown in Fig. 20.

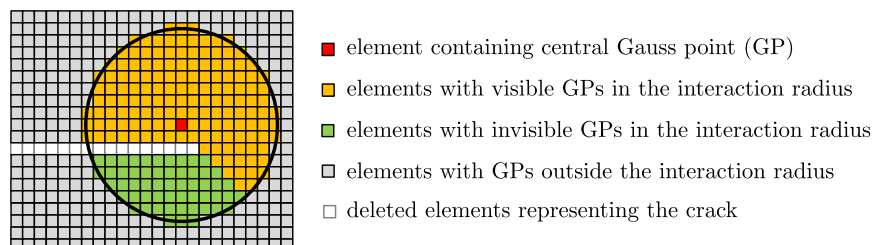


**Fig. 25.** A depiction of the visibility method implemented which is motivated by [54]. Besides the free surfaces produced by element deletion during virtual crack extension, without loss of generality the implementation is generalized to include any kind of nonconvexities in the problem boundary which naturally arises in the notched small punch test.

interaction radius. Consistently also for the unnotched cases uniform  $2.5 \mu\text{m}$  elements are used at crack regions.

The effect of the nonlocal operator on the resultant principal stress gradients is shown in Fig. 21 where the normalized principal stress distributions before and after delocalization are depicted for the notched and the unnotched cases for  $-196 \text{ }^\circ\text{C}$  and an interaction radius of  $7 \mu\text{m}$ . At the notch tip, the stress field shows a steep gradient. The delocalization has a strong effect even for the relatively small interaction radius selected. On the other hand, for the unnotched specimen, the effect of delocalization is hardly distinguishable.

Since the underlying mechanisms for the notched specimens are identical to those of the previous section, we confine ourselves to giving the crack patterns for the unnotched tests for the three temperatures  $-196 \text{ }^\circ\text{C}$ ,  $-158 \text{ }^\circ\text{C}$  and  $25 \text{ }^\circ\text{C}$  as depicted in Fig. 22. Large stresses needed for brittle fracture are achieved only at low temperatures. Otherwise, ductile fracture at high strains is observed. Similar to experimental findings, towards lower temperatures reduced bulging (i.e., decreasing amount of plastic deformation) is noted from the overall morphology of the fractured disks. In all cases the cracks start from the bottom surface of the disk and propagate towards the top face until complete separation. For  $-196 \text{ }^\circ\text{C}$ , a linear crack orthogonal to the disk propagates along the direction of maximum in-plane stress. Hence, fracture is of brittle Mode I with the total deformation for fracture being considerably lower than at  $-158 \text{ }^\circ\text{C}$  and  $25 \text{ }^\circ\text{C}$ . For  $25 \text{ }^\circ\text{C}$ , fracture takes place only after a considerable reduction in thickness in a ductile manner following a path parallel to the punch travel. For  $-158 \text{ }^\circ\text{C}$ , on the other hand, a kink is observed when the initially vertical crack takes an inclined direction.

While ductile fracture shows a ring-shaped pattern in the experimental results, brittle fracture propagation is not fully axisymmetric unlike the basic assumption which the current 2D model is based on. A 3D model with random material property distributions and some inevitable eccentricity of the puncher loading is expected to reproduce even better the fracture patterns. Nevertheless, the current modeling framework already provides various insights regarding the mechanisms of ductile and brittle fracture at much lower computational cost.

Fig. 23 illustrates the crack development for  $-158 \text{ }^\circ\text{C}$  and  $25 \text{ }^\circ\text{C}$ . In both cases, fracture starts with a severe strain localization due to void formation in a direction around  $45^\circ$  to the maximum principal stress direction. This ductile mode of fracture is preserved for  $25 \text{ }^\circ\text{C}$  until complete failure. However, for  $-158 \text{ }^\circ\text{C}$ , a transition from initially ductile to brittle fracture is observed with a considerably higher RKR integral at the crack tip as compared to  $25 \text{ }^\circ\text{C}$ . This transition creates a kink when the crack abruptly deflects to follow the normal of the maximum principal stress. As seen in Fig. 23(d) during the brittle cracking phase there is almost no void formation.

The punch force vs. displacement curves are compared with the experimental ones in Fig. 24. For  $-196 \text{ }^\circ\text{C}$ , the force–displacement curves as well as displacement to fracture agree reasonably well with experimental results. For the unnotched tests, there is some overestimation of the fracture displacements for  $-158 \text{ }^\circ\text{C}$  and

**Table 2**  
Elastic predictor–thermo-plastic corrector type operator split.

Total		Elastic predictor	+	Thermo-plastic corrector
$\begin{Bmatrix} \Delta \hat{\epsilon} \neq \mathbf{0} \\ \Delta \hat{\epsilon}_p \neq \mathbf{0} \\ \Delta \hat{\epsilon}_\theta \neq \mathbf{0} \\ \Delta \hat{\sigma} \neq \mathbf{0} \\ \Delta e_p \neq 0 \\ \Delta f \neq 0 \\ \Delta \theta \neq 0 \end{Bmatrix}$	=	$\begin{Bmatrix} \Delta \hat{\epsilon} \neq \mathbf{0} \\ \Delta \hat{\epsilon}_p = \mathbf{0} \\ \Delta \hat{\epsilon}_\theta = \mathbf{0} \\ \Delta \hat{\sigma} = C_e : \Delta \hat{\epsilon} \\ \Delta e_p = 0 \\ \Delta f = 0 \\ \Delta \theta = 0 \end{Bmatrix}$	+	$\begin{Bmatrix} \Delta \hat{\epsilon} = \mathbf{0} \\ \Delta \hat{\epsilon}_p \neq \mathbf{0} \\ \Delta \hat{\epsilon}_\theta \neq \mathbf{0} \\ \Delta \hat{\sigma} = -C_e : [\Delta \hat{\epsilon}_p + \Delta \hat{\epsilon}_\theta] \\ \Delta e_p \neq 0 \\ \Delta f \neq 0 \\ \Delta \theta \neq 0 \end{Bmatrix}$

**Table 3**  
Material parameters for small punch disks made of P91 steel. Values are given at  $T = \{-196 \text{ }^\circ\text{C}, -158 \text{ }^\circ\text{C}, 25 \text{ }^\circ\text{C}\}$ .

Parameter	Symbol	Value	Unit	Reference	
Thermal expansion coef.	$\alpha_\theta$	$1.3 \times 10^{-5}$	$\text{K}^{-1}$	Eq. (5)	
Melting temperature	$\theta_{\text{melt}}$	1717	K	Eq. (10)	
Reference temperature	$\theta_{\text{ref}}$	298	K	Eq. (10)	
Specific heat capacity	$c_p$	622	$\text{m}^2 \text{K}^{-1} \text{s}^{-2}$	Eq. (19)	
Taylor–Quinney coef.	$\chi$	0.9	[–]	Eq. (19)	
Density (initial)	$\rho$	$7.85 \times 10^{-9}$	$\text{t mm}^{-3}$	Eq. (19)	
Young's modulus	$E$	{234.9, 230.6, 210}	GPa	Eq. (4)	
Poisson's ratio	$\nu$	0.3	[–]	Eq. (4)	
Plastic hardening	$h_0$	123	MPa	Eq. (27)	
	$h_1$	75	MPa	Eq. (27)	
	$\sigma_{y0}$	520	MPa	Eq. (27)	
	$\sigma_{y1}$	376	MPa	Eq. (27)	
	$\sigma_{y\infty}$	831	MPa	Eq. (27)	
	$m$	6.14	[–]	Eq. (27)	
	$n$	0.541	[–]	Eq. (27)	
	$e_{p0}$	0.006	[–]	Eq. (27)	
	Temperature effect	$t_y(\theta)$	{1.54, 1.24, 1}	[–]	Eq. (8)
	Strain rate effect	$r_y(\dot{\epsilon}^p)$	1	[–]	Eq. (8)
Nonlocal GTN model	$(q_1 = 1/f_u^*, q_2, q_3)$	{1.5, 1.2, 25}	[–]	Eq. (6)	
	$f_0$	0.00044	[–]	Eq. (28)	
	$f_N$	0.02	[–]	Eq. (14)	
	$\epsilon_N$	0.3	[–]	Eq. (14)	
	$S_N$	0.1	[–]	Eq. (14)	
	$k_w$	0	[–]	Eq. (17)	
	$f_c$	0.1	[–]	Eq. (7)	
	$f_F$	0.25	[–]	Eq. (7)	
	$R_{\text{ductile}}$	{2.5, 5}	$\mu\text{m}$	Eq. (21)	
	Nonlocal RKR model <sup>a</sup>	$\sigma_c$	{2.83 $\sigma_{y0}$ , 2.55 $\sigma_{y0}$ }	MPa	Eq. (26)
		$R_{\text{brittle}}$	{7, 12.5}	$\mu\text{m}$	Eq. (24)

<sup>a</sup> For both the notched and unnotched cases the brittle fracture onset can be predicted reasonably well with  $(\sigma_c, R_{\text{brittle}}) = (2.83\sigma_{y0}, 7 \mu\text{m})$  for which  $R_{\text{ductile}} = 2.5 \mu\text{m} < R_{\text{brittle}}$  can be selected.

25 °C. Both curves show steep drops as a result of abrupt fracturing. A possible way to better capture ductile fracture strains for different temperatures might consist in a temperature dependent modification of the void kinetics in addition to the temperature dependence of plastic flow. However, this is beyond the scope of the current study. For –158 °C a significant divergence of the forces occurs after a punch displacement of about 0.7 mm. However, it is impossible to identify the source of this discrepancy on the base of a single experimental result.

The deformation energies for the unnotched tests computed for –196 °C, –158 °C and 25 °C are 472 Nmm, 2497 Nmm and 2057 Nmm, respectively, while experimental values are 499 Nmm, 1819 Nmm and 1916 Nmm. The unnotched tests are seen to require

considerably higher deformation energy until fracture. While the considerable differences in the energies required for brittle or ductile fracture are captured by the simulations, the energy required in the simulation at –158 °C is predicted to exceed that at room temperature. This relates to the delayed fracture for –158 °C as compared to the experimental findings.

## 6. Conclusion and outlook

Notwithstanding various experimental studies regarding the ductile–brittle transition temperature of small punch tests, there has been no attempt to estimate the transition temperature

numerically. In this study, a unified thermo-plastic constitutive model combining the RKR brittle damage approach with Gurson's porous plasticity was therefore established to predict the temperature dependent fracture behavior of notched and unnotched small punch specimens. Associated length scales are taken into account for both the ductile and brittle modes of fracture. A detailed parameter identification has been carried out for the corresponding constitutive behaviors. The model was validated by comparing experimental and numerical load–displacement curves as well as optical and SEM images of the fractured disks revealing the crack patterns and fracture surface morphologies. The results provide new insight into the application of a non-local formulation of brittle fracture under small-scale (notched specimens) and large-scale yielding conditions (unnotched specimens). The model developed will be instrumental in the further analysis of the effects of strain rate, different notch and puncher head geometries on small punch transition temperature.

The application of the present numerical modeling scheme to small punch testing constitutes a novel approach which is expected to impact model validation and calibration in general: as a matter of fact, the small punch test is most sensitive as a model validation tool owing to its multi-axiality and loading history. This is even more true as different specimen geometries – notched and unnotched – are considered. At the same time, from an experimental point of view it only requires tiny amounts of material and, therefore, is almost non-destructive. Further, specimens are easy (and cheap) to manufacture, and the experimental setup is comparatively simple.

## Acknowledgment

Financial support of this work has been provided by the German Research Foundation DFG PAK250, TP4. This support is gratefully acknowledged.

## Appendix A. Numerical implementation

The ABAQUS implementation of the nonlocal framework is handled in two parts. In the first part a local return mapping algorithm is applied via the VUMAT subroutine interface. The void volume fraction increments and the maximum principal stresses are saved at the end of the time step. These are then used through the VUSDFLD subroutine for the computation of the nonlocal counterparts. At the beginning of the following time step, the local void volume fraction increments are replaced by their nonlocal counterparts.

### A.1. Local integration algorithm

Due to the reasons given in Section 5,  $\mathbf{q} = \mathbf{0}$  is assumed and the global heat flux problem is not solved. The remaining system could be solved locally assuming adiabatic conditions. For the sake of completeness, the adiabatic implementation is given. Isothermal conditions are met for  $\chi = 0$ . The complete set of equations reads:

$$\left. \begin{aligned} \dot{\hat{\mathbf{e}}}_e &= \dot{\hat{\mathbf{e}}} - \dot{\hat{\mathbf{e}}}_p - \dot{\hat{\mathbf{e}}}_\theta, \\ \dot{\hat{\mathbf{e}}}_p &= \dot{\gamma} \partial_{\hat{\sigma}} \Phi_p, \\ \dot{\hat{\mathbf{e}}}_\theta &= \alpha_\theta \dot{\Theta} \mathbf{1}, \\ \dot{\hat{\sigma}} &= \mathbb{C}_e : \dot{\hat{\mathbf{e}}}_e, \\ \dot{e}_p &= \dot{\gamma} \eta : \partial_{\hat{\sigma}} \Phi_p, \\ \dot{f} &= \dot{\gamma} [A_N \boldsymbol{\eta} + \mathbf{B}_G] : \partial_{\hat{\sigma}} \Phi_p, \\ \dot{\Theta} &= \dot{\gamma} [\chi / \rho c_p] \hat{\sigma} : \partial_{\hat{\sigma}} \Phi_p. \end{aligned} \right\} \quad (29)$$

$\boldsymbol{\eta} := \hat{\sigma} / [[1-f]\sigma_y]$  and  $\mathbf{B}_G = \mathbf{B}_G(f, \sigma_D)$  is defined as

$$\mathbf{B}_G := [1-f] \mathbf{1} + k_w f \frac{W(\hat{\sigma}_D)}{\sigma_{eq}} \hat{\sigma}_D. \quad (30)$$

For solving Eqs. (29), an elastic predictor-thermo-plastic corrector type of algorithm is used. Letting  $\Delta(\bullet) = \Delta t \times (\bullet)$ , the subscript  $n+1$  denotes the (unknown) step at time  $t_{n+1}$  and  $n$  denotes the (known) step at time  $t_n$ , the solution  $\{\hat{\sigma}_{n+1}, e_{p,n+1}, f_{n+1}, \Theta_{n+1}\}$  is sought for the given  $\{\hat{\sigma}_n, e_{p,n}, f_n, \Theta_n\}$  and the strain increment  $\Delta \hat{\mathbf{e}}$  with  $\Delta t = t_{n+1} - t_n$ . The corresponding operator-split is summarized in Table 2.

**Elastic predictor:** Here, a trial step is realized assuming that the strain increment  $\Delta \hat{\mathbf{e}}$  is purely elastic. Once the corresponding value of the flow potential is smaller than zero, i.e.,  $\Phi_{p,n+1,trial} < 0$ , the trial step is assumed to be correct, otherwise a thermo-plastic correction is required.

**Thermo-plastic corrector:** The semi-implicit thermo-plastic corrector algorithm relies on exploitation of the first-order Taylor series expansion of the yield potential around a known step  $\langle i \rangle$

$$\begin{aligned} \Phi_{p,n+1}^{(i+1)} &\approx \Phi_{p,n+1}^{(i)} + \mathbf{r}_{n+1}^{(i)} : \delta \hat{\sigma}_{n+1}^{(i)} \\ &\quad + \xi_{n+1}^{(i)} \delta e_{p,n+1}^{(i)} + \varsigma_{n+1}^{(i)} \delta f_{n+1}^{(i)} + \varpi_{n+1}^{(i)} \delta \dot{e}_{p,n+1}^{(i)} \\ &\quad + \mu_{n+1}^{(i)} \delta \Theta_{n+1}^{(i)}, \end{aligned} \quad (31)$$

where

$$\left. \begin{aligned} \mathbf{r} &:= \partial_{\hat{\sigma}} \Phi_p = \partial_{\sigma_{eq}} \Phi_p \partial_{\hat{\sigma}} \sigma_{eq} + \partial_{\sigma_m} \Phi_p \partial_{\hat{\sigma}} \sigma_m, \\ \xi &:= \partial_{e_p} \Phi_p = \partial_{\sigma_y} \Phi_p \partial_{e_p} \sigma_y, \\ \varsigma &:= \partial_f \Phi_p = 2q_1 \cosh(3/2 [q_2 \sigma_m / \sigma_y]) - 2fq_3, \\ \varpi &:= \partial_{\dot{e}_p} \Phi_p = \partial_{\sigma_y} \Phi_p \partial_{\dot{e}_p} \sigma_y, \\ \mu &:= \partial_{\Theta} \Phi_p = \partial_{\sigma_y} \Phi_p \partial_{\Theta} \sigma_y. \end{aligned} \right\} \quad (32)$$

The increments  $\delta(\bullet)^{(i)} = (\bullet)^{(i+1)} - (\bullet)^{(i)}$  in Eq. (31) read

$$\left. \begin{aligned} \delta \hat{\sigma}_{n+1}^{(i)} &= -\delta \gamma_{n+1}^{(i)} \mathbb{C}_e : \left[ \mathbf{r}_{n+1}^{(i)} + \alpha_\theta \chi / [\rho c_p] [\hat{\sigma}_{n+1}^{(i)} : \mathbf{r}_{n+1}^{(i)}] \mathbf{1} \right], \\ \delta e_{p,n+1}^{(i)} &= \delta \gamma_{n+1}^{(i)} \boldsymbol{\eta}_{n+1}^{(i)} : \mathbf{r}_{n+1}^{(i)} \\ \delta f_{n+1}^{(i)} &= \delta \gamma_{n+1}^{(i)} [A_{N,n+1}^{(i)} \boldsymbol{\eta}_{n+1}^{(i)} + \mathbf{B}_{G,n+1}^{(i)}] : \mathbf{r}_{n+1}^{(i)} \\ \delta \dot{e}_{p,n+1}^{(i)} &= \delta e_{p,n+1}^{(i)} / \Delta t \\ \delta \Theta_{n+1}^{(i)} &= \delta \gamma_{n+1}^{(i)} \chi / [\rho c_p] \hat{\sigma}_{n+1}^{(i)} : \mathbf{r}_{n+1}^{(i)}. \end{aligned} \right\} \quad (33)$$

Using the condition  $\Phi_{p,n+1}^{(i+1)} = 0$  as required, and substituting Eq. (31) into the right-hand side of Eq. (33) which allows factoring out the incremental plasticity parameter, we find  $\delta \gamma_{n+1}^{(i)}$  as

$$\delta \gamma_{n+1}^{(i)} = \frac{\Phi_{p,n+1}^{(i)}}{\mathbf{r}_{n+1}^{(i)} : [\mathbb{C}^e : A_{n+1}^{(i)} + D_{n+1}^{(i)}]}, \quad (34)$$

where

$$\mathbf{A}_{n+1}^{(i)} = \mathbf{r}_{n+1}^{(i)} + \alpha_\theta \chi / [\rho c_p] [\hat{\sigma}_{n+1}^{(i)} : \mathbf{r}_{n+1}^{(i)}] \mathbf{1}, \quad (35)$$

and

$$\begin{aligned} \mathbf{D}_{n+1}^{(i)} &= \left[ \xi_{n+1}^{(i)} + \frac{\varpi_{n+1}^{(i)}}{\Delta t} \right] \boldsymbol{\eta}_{n+1}^{(i)} + \varsigma_{n+1}^{(i)} [A_{N,n+1}^{(i)} \boldsymbol{\eta}_{n+1}^{(i)} + \mathbf{B}_{G,n+1}^{(i)}] \\ &\quad + \mu_{n+1}^{(i)} \frac{\chi}{\rho c_p} \hat{\sigma}_{n+1}^{(i)}. \end{aligned} \quad (36)$$

We start the iterations by assigning an initial guess to the plastic multiplier  $\Delta \gamma_{n+1}^{(0)}$ . This depends on the rate dependence of hardening which is assumed to vanish for  $\dot{e}_p < \dot{e}_{p0}$ , that is  $r_y = 1$  as  $\dot{e}_p < \dot{e}_{p0}$ . The consequent numerical difficulty pertaining to the hardening discontinuity is remedied following the lines of [53].

Consequently, once  $\Phi_p(\Delta t \times \dot{\epsilon}_{p0}) > 0$  we use the initial guess  $\Delta \gamma_{n+1}^{(0)} = \Delta t \times \dot{\epsilon}_{p0}$ , otherwise  $\Delta \gamma_{n+1}^{(0)} = 0$ . State variable updates  $(\bullet)^{(i+1)} = (\bullet)^{(i)} + \delta(\bullet)^{(i)}$  are continued throughout the iterations  $\langle i \rangle$  for the computed increment of the plastic multiplier in Eq. (34), until  $\phi_{p,n+1}^{(i+1)} \approx 0$  to a desired accuracy. The stress tensor is then rotated back to the current coordinates:  $\sigma_{n+1} = \mathbf{R}_{n+1} \cdot \hat{\sigma}_{n+1} \cdot \mathbf{R}_{n+1}^T$ .

### A.2. Nonlocal averaging

The implementation of the nonlocal averaging is realized over the time discrete form of the void volume fraction rate and the principal stress components using the VUSDFLD subroutine interface of ABAQUS. The integration is supplied using Gaussian quadrature over the material points inside the nonlocal volume of interaction.

A drawback of the nonlocal averaging schemes is associated with the boundary nonconvexity. Nonconvexity can occur due to specimen geometry as well as newly produced surfaces from crack propagation. Such nonconvexities render the interaction among material points at opposing sides of the discontinuity questionable due to the long range interactions of the microcracks with each other related to the high scattering effects of the elastic waves. In order to circumvent this problem a visibility criterion, similar to the one presented in [54] within the context of meshless methods, is applied for both brittle and ductile damage processes. Accordingly, Gauss points blocked by the existence of a free surface either due to an extended crack or nonconvex boundary surface are excluded from the interaction vector of the receiver Gauss point even if they are within the interaction radius (Eq. (25)).

## References

- [1] Needleman A, Tvergaard V. Numerical modeling of the ductile–brittle transition. *Int J Fract* 2000;101:73–97.
- [2] Manahan M, Argon A, Harling O. The development of a miniaturized disk bend test for determination of post irradiation mechanical properties. *J Nucl Mater* 1981;104:1545–50.
- [3] Gülçimen B, Durmuş A, Ülkü S, Hurst R, Turba K, Hähner P. Mechanical characterisation of a P91 weldment by means of small punch fracture testing. *Int J Press Vessels Pip* 2013; 105–106: 28–35.
- [4] Baik J, Kameda J, Buck O. Development of small punch tests for ductile–brittle transition temperature measurement of embrittled Ni–Cr steels. *ASTM STP* 888-EB; 1986. p. 92–111.
- [5] Norris S. A comparison of the disk bend test and the Charpy impact test for fracture property evaluation of power station steels. *Int J Press Vessels Pip* 1997;74:135–44.
- [6] Ha J, Fleury E. Small punch tests to estimate the mechanical properties of steels for steam power plant: II. Fracture toughness. *Int J Press Vessels Pip* 1998;75:707–13.
- [7] Zidan A, Brookfield J. A technique for the determination of post-yield material properties from the small punch test. *J Strain Anal Eng Des* 2003;38(4):367–76.
- [8] CEN Workshop Agreement. Small punch test method for metallic materials., Technical report CWA 15627; 2006.
- [9] Nahshon K, Hutchinson J. Modification of the Gurson model to shear failure. *Eur J Mech A/Solids* 2008;27:1–17.
- [10] Ritchie R, Knott J, Rice J. On the tensile relationship between critical tensile stress and fracture toughness in mild steel. *J Mech Phys Solids* 1973;21:395–410.
- [11] Gurson A. Continuum theory of ductile rupture by void nucleation and growth –Part I. Yield criteria and rules for porous ductile media. *J Eng Mater Technol* 1977;99:2–15.
- [12] Tvergaard V. Influence of voids on shear band instabilities under plane strain conditions. *Int J Fract* 1981;17:389–407.
- [13] Tvergaard V. On localization in ductile materials containing spherical voids. *Int J Fract* 1982;18:237–52.
- [14] Tvergaard V, Needleman A. Analysis of the cup-cone fracture in a round tensile bar. *Acta Metall* 1984;32:157–69.
- [15] Wang W, Sluys L, de Borst R. Viscoplasticity for instabilities due to strain softening and strain-rate softening. *Int J Numer Methods Eng* 1997;40:3839–64.
- [16] Chu C, Needleman A. Void nucleation effects in biaxially stretched sheets. *J Eng Mater Technol* 1980;102:249–56.
- [17] Bao Y, Wierzbicki T. On fracture locus in the equivalent strain and stress triaxiality space. *Int J Mech Sci* 2004;46:81–98.
- [18] Barsoum I, Faleskog J. Rupture in combined tension and shear: experiments. *Int J Solids Struct* 2007;44:1768–86.
- [19] Taylor G, Quinney H. The latent energy remaining in a metal after cold working. *Proc R Soc Lond* 1934;143(849):307–26.
- [20] Bazant Z, Belytschko T, Chang T. Continuum theory for strain softening. *J Eng Mech Div ASCE* 1984;110(12):1666–92.
- [21] Linse GH, Kuna M. Simulation of crack propagation using a gradient-enriched ductile damage model based on dilatational strain. *Eng Fract Mech* 2012; 95: 13–28 [Cracks in microstructures and engineering components]. <http://dx.doi.org/http://dx.doi.org/10.1016/j.engfractmech.2012.07.004>. (<http://www.science-direct.com/science/article/pii/S0013794412002809>).
- [22] Tvergaard V, Needleman A. Effects of nonlocal damage in porous plastic solids. *Int J Solids Struct* 1995;32:1063–77.
- [23] Needleman A, Tvergaard V. Dynamic crack growth in a nonlocal progressively cavitating solid. *Eur J Mech A/Solids* 1998;17(3):421–38.
- [24] Pijaudier-Cabot G, Bazant Z. Nonlocal damage theory. *J Eng Mech ASCE* 1987;113(10):1512–33.
- [25] Leblond J, Perrin G, Devaux J. Bifurcation effects in ductile metals with damage delocalization. *J Appl Mech* 1994;61:236–42.
- [26] Beremin F. A local criterion for cleavage fracture of a nuclear pressure vessel steel. *Metall Trans* 1983;14A:2277–87.
- [27] Mudry F. A local approach to cleavage fracture. *Nucl Eng Des* 1987;105:65–76.
- [28] Andrieu A, Pineau A, Besson J, Ryckelynck D, Bouaziz O. Bimodal beremin-type model for brittle fracture of inhomogeneous ferritic steels: theory and applications. *Eng Fract Mech* 2012;95:84–101 [Cracks in microstructures and engineering components]. <http://dx.doi.org/10.1016/j.engfractmech.2011.10.016>. (<http://www.sciencedirect.com/science/article/pii/S0013794412002068>).
- [29] Volokh KY. Non-linear thermoelasticity with energy limiters. *Int J Non-Linear Mech* 2015;76:169–75.
- [30] Lemaitre J. *A course on damage mechanics*. Berlin: Springer-Verlag; 1996.
- [31] Soyarslan C, Türtük I, Deliktas B, Bargmann S. A thermodynamically consistent constitutive theory for modeling micro-void and/or micro-crack driven failure in metals at finite strains. *Int J Appl Mech*; 2015, accepted for publication.
- [32] Miehe C, Hofacker M, Schnelz L-M, Aldakheel F. Phase field modeling of fracture in multi-physics problems. Part II: coupled brittle-to-ductile failure criteria and crack propagation in thermo-elastic plastic solids. *Comput Methods Appl Mech Eng* 2015;294:486–522. <http://dx.doi.org/10.1016/j.cma.2014.11.017>. (<http://www.sciencedirect.com/science/article/pii/S0045782514004435>).
- [33] Duda FP, Ciaronetti A, Sánchez PJ, Huespe AE. A phase-field/gradient damage model for brittle fracture in elastic-plastic solids. *Int J Plast* 2015; 65: 269–96. <http://dx.doi.org/http://dx.doi.org/10.1016/j.iijplas.2014.09.005>. (<http://www.sciencedirect.com/science/article/pii/S0749641914001892>).
- [34] Hütter G, Linse T, Roth S, Mühlich U, Kuna M. A modelling approach for the complete ductile-to-brittle transition region: cohesive zone in combination with a non-local Gurson-model. *Int J Fract* 2014;185:129–53.
- [35] Klueh R, Nelson A. Ferritic/martensitic steels for next-generation reactors. *J Nucl Mater* 2007;371:37–52.
- [36] Mao X, Takahashi H. Development of a further-miniaturized specimen of 3 mm diameter for TEM disk ( $\phi$  3 mm) small punch tests. *J Nucl Mater* 1987;150(1):42–52.
- [37] Lee J, Kim I, Kimura A. Application of small punch test to evaluate sigma-phase embrittlement of pressure vessel cladding material. *J Nucl Sci Technol* 2003;40:664–71.
- [38] Hamdane O, Bouquerel J, Proriot-Serre I, Vogt J-B. Effect of heat treatment on liquid sodium embrittlement of T91 martensitic steel. *J Mater Process Technol* 2011;211:2085–90.
- [39] Turba K, Gülçimen B, Li Y, Blagoeva D, Hähner P, Hurst R. Introduction of a new notched specimen geometry to determine fracture properties by small punch testing. *Eng Fract Mech* 2011;78(16):2826–33.
- [40] Chatterjee A, Chakrabarti D, Moitra A, Bhaduri A. Effect of normalization temperatures on ductile–brittle transition temperature of a modified 9Cr–1Mo steel. *Mater Sci Eng A* 2014;618:219–31.
- [41] Thyssen Krupp Materials International. Material data sheet - alloy steel tubes for high-temperature service. Technical report, Material data sheet P91/T91 10/2011; 2011.
- [42] Jia X, Dai Y. Small punch tests on martensitic/ferritic steels F82H, T91 and Optimax-A irradiated in SINQ Target-3. *J Nucl Mater* 2003;323:360–7.
- [43] Choudhary B, Rao Palaparti D, Samuel I. Analysis of tensile stress–strain and work-hardening behavior in 9Cr–1Mo ferritic steel. *Metall Mater Trans A* 2013;44:212–23.
- [44] Shashank Dutt B, Nani Babu M, Venugopal S, Sasikala G, Bhaduri A. Effect of test temperature on fracture toughness of modified 9Cr–1Mo steel. *Mater Sci Technol* 2011;27(10):1527–33.
- [45] Franklin AG. Comparison between a quantitative microscope and chemical methods for assessment of non-metallic inclusions. *J Iron Steel Inst* 1969;207:181–6.
- [46] Abendroth M, Kuna M. Determination of deformation and failure properties of ductile materials by means of the small punch test and neural networks. *Comput Mater Sci* 2003;28:633–44.
- [47] Abendroth M, Kuna M. Identification of ductile damage and fracture parameters from the small punch test using neural networks. *Eng Fract Mech* 2006;73:710–25.
- [48] Lee J-S, Jang J-I, Lee B-W, Choi Y, Lee SG, Kwon D. An instrumented indentation technique for estimating fracture toughness of ductile materials: a critical indentation energy model based on continuum damage mechanics. *Acta Mater* 2006;54:1101–9.

- [49] Brown L, Embury J. The initiation and growth of voids at second phase particles. In: Proceedings of the third international conference on the strength of metals and alloys. Institute of Metals, London, vol. 25(3); 1973. p. 164.
- [50] Xia L, Fong Shih C. A computational approach to ductile crack growth under large scale yielding conditions. *J Mech Phys Solids* 1995;43(3):389–413.
- [51] Xia L, Shih Fong C. Ductile crack growth-III. Transition to cleavage fracture incorporating statistics. *J Mech Phys Solids* 1996;44(4):603–39.
- [52] ABAQUS Documentation. Dassault Systèmes, Providence, RI, USA. Technical report; 2012.
- [53] Zaera R, Fernandez Saez J. An implicit consistent algorithm for the integration of thermoviscoplastic constitutive equations in adiabatic conditions and finite deformations. *Int J Solids Struct* 2006;43(6):1594–612.
- [54] Belytschko T, Lu YY, Gu L. Element-free Galerkin methods. *Int J Numer Methods Eng* 2004;37:229–56.